https://doi.org/10.5194/wes-2026-214
Preprint. Discussion started: 19 November 2026
© Author(s) 2026. CC BY 4.0 License.



eawe european academy of wind energy
Open Access WIND ENERGY SCIENCE DISCUSSIONS

Combined wake steering and helix control: why power gains are not additive

Simone Tamaro[1], Franz V. Mühle[1], Brian Dsouza[2], Davide Bortolin[1], İris Alagöz[1], Filippo Campagnolo[1], Marinos Manolesos[3], Andrea Sciacchitano[2], and Carlo Luigi Bottasso[1]

[1]Wind Energy Institute, Technical University of Munich, 85748 Garching b. München, Germany
[2]Faculty of Aerospace Engineering, Delft University of Technology, Delft, South Holland, The Netherlands
[3]School of Mechanical Engineering, National Technical University of Athens, Ir. Politechniou 9, Zografou 15772, Athens, Greece

Correspondence: Franz V. Mühle (franz.muehle@tum.de)

Abstract. Combining wake steering with wake mixing appears to be a natural strategy for boosting the power of a wind farm. However, our experiments show that this seemingly straightforward combination does not provide the expected benefits, highlighting that the interaction between steering and mixing is more complex than anticipated. We investigate this interaction through two dedicated wind-tunnel experiments. The first experimental campaign evaluates the impact of the combined strategy on the performance of a small wind turbine cluster, while the second employs Lagrangian particle tracking (LPT) to investigate the underlying wake dynamics. The combined control strategy is compared with greedy control, pure wake steering, and pure helix control.

The wind turbine cluster experiments show that the benefits of wake steering and helix control are not additive, and the combined strategy provides no advantage over the individual control techniques. The LPT measurements reveal a reduction in both wake meandering and lateral wake deflection when helix control and wake steering are applied simultaneously. The flow measurements further indicate that interactions between the vortical structures generated by the two control strategies are responsible for this behavior, providing a physical explanation for the reduced performance of the combined approach. The proposed vortex-interaction mechanism is further tested using large-eddy simulations coupled with the actuator line method (LES-ALM) for the opposite yaw direction, which was not investigated experimentally.

While the combined strategy does not enhance power output, this negative result reveals a critical physical limitation in combined wake-control design, demonstrating that individual control effects cannot simply be superimposed in engineering models.

1 Introduction

Wake mixing has recently gained significant attention in the context of wind farm control. It involves operating rotor actuators in non-standard ways to enhance wake recovery, ultimately benefiting downstream turbines. Studies by Taschner et al. (2024); Bortolin et al. (2026) have shown that the effectiveness of wake mixing can rival, and in some cases exceed, that of the well-

https://doi.org/10.5194/wes-2026-214
Preprint. Discussion started: 19 November 2026
© Author(s) 2026. CC BY 4.0 License.



eawe european academy of wind energy
Open Access WIND ENERGY SCIENCE DISCUSSIONS

established wake steering approach (Medici and Alfredsson, 2006; Jiménez et al., 2010; Fleming et al., 2014; Doekemeijer et al., 2021), thereby sparking considerable interest in the research community.

One of the most prominent wake mixing strategies is the "helix" approach, which is a particular form of individual pitch control (IPC) that results in a helical path of the wake. In the helix approach, the pitch of each blade follows a sinusoidal motion with a constant phase offset among blades (Frederik, 2021). This actuation produces a rotating aerodynamic loading of the rotor, generating a rotating perturbation of the wake. The resulting helical wake structure enhances turbulent mixing and accelerates wake recovery (Mühle et al., 2024; Coquelet et al., 2024; Gutknecht et al., 2025b). As with wake steering, wake mixing presents a trade-off between the power loss at the actuated turbine upstream and the power gain observed downstream. This trade-off results in optimal combinations of actuation frequency and amplitude (Frederik, 2021; Mühle et al., 2024). Recent investigations have demonstrated wind farm power gains of up to +7.5% numerically (Frederik et al., 2020) and +8.7% experimentally (van der Hoek et al., 2024) on small clusters of two aligned rotors. Importantly, these gains have primarily been demonstrated for aligned, fully waked configurations, where helix control has been shown to outperform wake steering. Outside full wake alignment, however, the relative benefit of helix control is substantially less pronounced (Bortolin et al., 2026). Recent studies have also expanded the application of this method (van den Berg et al., 2022; van Vondelen et al., 2025) by synchronizing the actuation of two aligned rotors, which further improves the power gains.

Although the effectiveness of helix and wake steering alone has been extensively demonstrated, few studies have investigated their combined application. In principle, the two control strategies can be superimposed because they rely on different actuators: wake steering uses yaw misalignment, whereas helix control uses individual pitch control. Their combination is therefore an attractive prospect for wind farm control, with the potential to simultaneously redirect wakes away from downstream turbines while enhancing wake recovery. Moreover, the recent implementation of helix control in FLORIS (Gebraad et al., 2016) with the "Empirical Gauss" wake model, enables optimization studies that combine the two strategies, despite the lack of a detailed physical understanding of their interaction.

However, the apparent simplicity of combining wake steering and wake mixing masks a more complex interaction between the flow structures generated by the two strategies. In fact, the results presented in this work show that their effects are not additive and that the combined strategy does not provide an additional power benefit over the individual control strategies. This negative result is nevertheless important because the combination of wake steering and wake mixing represents an intuitively attractive and seemingly straightforward extension of existing control approaches. Demonstrating that these strategies can interfere with one another highlights a limitation that may otherwise be overlooked in wind farm control design and low-fidelity wake models.

The present work investigates this interaction through two complementary wind tunnel campaigns. The first evaluates the impact of combining wake steering and helix control on the power production of a small wind turbine cluster, comparing the combined strategy against greedy operation, wake steering alone, and helix control alone. The second employs three-dimensional Lagrangian particle tracking (LPT) to investigate the flow physics underlying the observed performance. The measurements reveal that the outer vortex generated by the helix interacts with the counter-rotating vortices generated by wake steering, altering the trajectory of the outer vortex and breaking the balance of the steering vortex pair. Based on this

https://doi.org/10.5194/wes-2026-214
Preprint. Discussion started: 19 November 2026
© Author(s) 2026. CC BY 4.0 License.



eawe european academy of wind energy
Open Access WIND ENERGY SCIENCE DISCUSSIONS

experimental observation, we propose a physical explanation for the lack of performance gains in terms of vortex interactions. This hypothesis is then tested using large-eddy simulations coupled with the actuator line method (LES-ALM) for the opposite yaw direction – a configuration not investigated experimentally – to assess whether reversing the yaw-induced vortex pair reverses the preferential path of the outer helix vortex, as predicted by the proposed mechanism.

The paper is structured as follows. Section 2 describes the two experimental facilities and the corresponding measurement and control approaches. Section 3 presents the experimental results. Section 3.1 includes the small wind farm power measurements, while Sect. 3.2 examines the three-dimensional wake dynamics from the LPT campaign alongside the supplementary numerical test. Finally, Sect. 4 summarizes the main findings and discusses their implications for combined wake-control strategies.

2 Experimental setup

In this work, the G1 wind turbine by Bottasso and Campagnolo (2022) is used. The G1 is a scaled turbine model with a diameter of $1.1D$, equipped with pitch and yaw actuators and a variable-speed generator. The turbine blades are designed for low Reynolds number operation due to the well-known lack of similarity in the wind tunnel (Wang et al., 2020; Bottasso and Campagnolo, 2022). The wake shed by the G1 was found to be rather similar to full-scale rotors by Wang et al. (2021). The G1 has a rated rotational speed $\Omega_R = 850$ RPM, rated wind speed of $U_{\infty,R} = 5.7$ ms^{-1}, and in these conditions it generates 46 W of power, P_R. Due to scaling, the G1 has a time scale factor of approximately 80 (Canet et al., 2021; Bottasso and Campagnolo, 2022) compared to a full-scale rotor, which means that time flows much faster in the experiment than in full-scale reality. Each blade pitch is controlled with a brushed motor *DCX16L GB SL 24V* located in the root section. The system includes a planetary head gearbox, an encoder, a Hall sensor, and a preload torsion spring, and it is described in Campagnolo et al. (2026).

2.1 Wind tunnel campaign I: wind turbine cluster power

A first wind tunnel campaign was conducted in the boundary-layer wind tunnel at the Politecnico di Milano (POLIMI), which is a closed-loop facility. The test section is 35.6 m long, and features a width of 13.84 m and a height of 3.84 m. Two G1 rotors (Bottasso and Campagnolo, 2022) were installed at a distance of $5D$ from each other and aligned with the inflow. The blockage factor is 1.8%. The most upstream rotor is installed at a distance $x_{\mathrm{WT}_1} \approx 21D$ from the inlet. The rotors are labeled WT_1 (upstream) and WT_2 (downstream). At the inlet of the test section, a set of 14 trapezoidal spires is installed to perturb the flow, resulting in a moderately turbulent inflow with a hub height turbulence intensity of approximately 6% measured at the WT_1 location, and a power law exponent of 0.14 for the vertical shear (Campagnolo et al., 2026). Figure 1 shows the wind tunnel setup.

The goal of this experiment is to determine the performance of the rotors under different control strategies. The following scenarios are considered:

- **Baseline**: both rotors operate with the control setpoints that maximize the power coefficient, i.e. collective blade pitch $\beta_{\mathrm{OPT}} = 0.4°$ and tip-speed ratio $\lambda = \Omega_R R/U_\infty = 8.5$.

https://doi.org/10.5194/wes-2026-214
Preprint. Discussion started: 19 November 2026
© Author(s) 2026. CC BY 4.0 License.

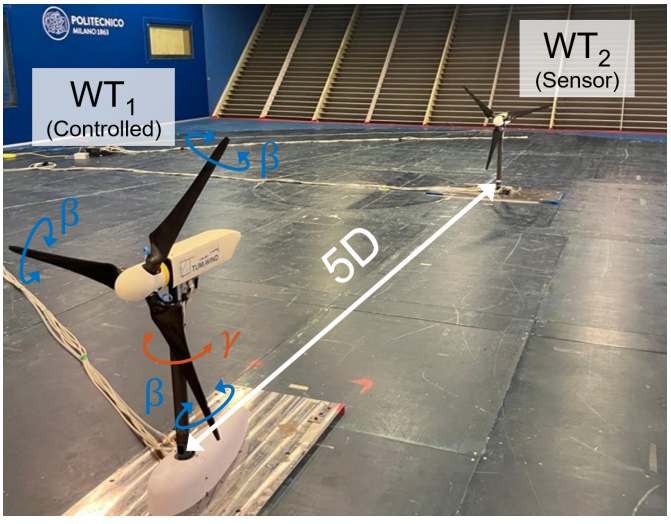


Figure 1. Experimental setup of wind tunnel campaign I. Two G1 scaled wind turbine models are aligned with the incoming flow and separated by a streamwise distance of $5D$. The upstream turbine, WT_1, is operated with prescribed yaw misalignment γ, constant rotor speed, and either fixed or time-varying blade pitch angle β, depending on the control strategy. The downstream turbine, WT_2, is operated in greedy mode and serves to quantify the impact of the upstream control strategy on wake recovery and power production.

- **Wake steering**: the front turbine is misaligned by a yaw angle γ. A yaw angle of $\gamma = -20°$ is selected because it provides a representative and clearly measurable wake-steering effect, corresponding to an overall power gain of approximately +2% under full wake impingement. Although only one wake-steering condition is considered, the objective here is not to characterize the dependence of the combined strategy on yaw angle, but to investigate the interaction between wake steering and helix control under a representative steering condition. The sign of γ is positive when the turbine rotates in the anti-clockwise direction when seen from the top.

- **Helix**: the helix is executed by imposing the following pitch angle $\boldsymbol{\beta}$ to the i-th blade

$$\beta_i = \beta_{\mathrm{OPT}} + A \sin\left(k\Omega_R t + \frac{2\pi}{3} i\right) \qquad \text{with } i = [0, 1, 2].$$

  We used an amplitude $A = 3°$ and a factor $k = 0.82$ from Mühle et al. (2024), which coincides with the so-called "clockwise helix" due to the direction of rotation impressed on the wake. This rotation direction was selected to reflect realistic operating conditions, as it is associated with a lower actuator duty cycle and reduced fatigue compared with the counterclockwise helix. The resulting period of excitation of the helix is

$$T_h = \frac{60}{(1-k)\Omega_R} = 0.39\,\mathrm{s}.$$

- **Wake steering + helix**: this scenario consists of applying the helix to the misaligned rotor. The procedure is straightforward because the actuators required for wake steering and the helix are independent.

https://doi.org/10.5194/wes-2026-214
Preprint. Discussion started: 19 November 2026
© Author(s) 2026. CC BY 4.0 License.



eawe european academy of wind energy
Open Access WIND ENERGY SCIENCE DISCUSSIONS

In all cases, the upstream rotor is operated at a constant rotational speed of $\Omega_R = 850$ RPM, while the downstream rotor operates at maximum power coefficient C_P through a standard greedy power controller. Normally, however, the yaw misalignment or activation of the helix would cause a reduction of Ω_R. Hence, we also include the results obtained with variable rotational speed on WT_1 in Appendix A. Although the fixed rotational speed is not necessarily realistic, we present it here as it matches the testing conditions used in wind tunnel campaign II, where it was necessary to synchronize the rotor with the flow measurement system. We summarize the control inputs in Table 1.

Table 1. Control inputs applied in the four control strategies: tip-speed ratio λ, blade pitch angle $\boldsymbol{\beta}$, and misalignment yaw angle γ.

	Baseline	Helix	Wake steering	Wake steering + helix
λ	8.5	8.5	8.5	8.5
$\boldsymbol{\beta}$	β_{OPT}	$\beta_{\mathrm{OPT}} + A\sin\left(k\Omega_R t + \left[0,\ \frac{2\pi}{3},\ \frac{4\pi}{3}\right]\right)$	β_{OPT}	$\beta_{\mathrm{OPT}} + A\sin\left(k\Omega_R t + \left[0,\ \frac{2\pi}{3},\ \frac{4\pi}{3}\right]\right)$
γ	0°	0°	-20°	-20°

2.2 Wind tunnel campaign II: wake characterization

The second wind tunnel campaign aims to measure the flow in the wake of a G1 under the four control scenarios described in the previous section. A single G1 turbine is installed in the Open Jet Facility (OJF) at the TU Delft Aerospace Engineering Laboratories. The OJF is an atmospheric closed-circuit open-jet wind tunnel with an octagonal exit section of 2.85×2.85 m^2 (Lignarolo et al., 2014). The freestream velocity was set to $U_\infty = 5.7$ ms^{-1}, corresponding to the rated wind speed of the G1.

The flow was measured using three-dimensional LPT, which consists of four high-speed cameras (Photron Mini AX100) for image acquisition and arrays of LEDs (LED-Flashlight 300 blue, LaVision GmbH) for illumination. Neutrally buoyant helium-filled soap bubbles were used as tracer particles and generated as described by Scarano et al. (2015); Faleiros et al. (2019). The in-house-developed seeding system comprises 400 seeding generators, each producing nominally 30,000 bubbles/sec. The resulting measurement volume is approximately $300 \times 600 \times 400$ mm^3 (depth $\times$ width $\times$ height), covering one half of the rotor. The imaging system specifications are tabulated in Table 2, while Fig. 2 illustrates the experimental setup.

Table 2. Imaging system specifications used for the LPT measurements.

Camera	Photron Mini AX100
Sensor size	1024 px $\times$ 1024 px
Acquisition frequency	600 Hz
Lens focal length, f	60 mm
$f\#$	11
Field of view	$300 \times 600 \times 400$ mm^3 (depth$\times$width$\times$height)

https://doi.org/10.5194/wes-2026-214
Preprint. Discussion started: 19 November 2026
© Author(s) 2026. CC BY 4.0 License.

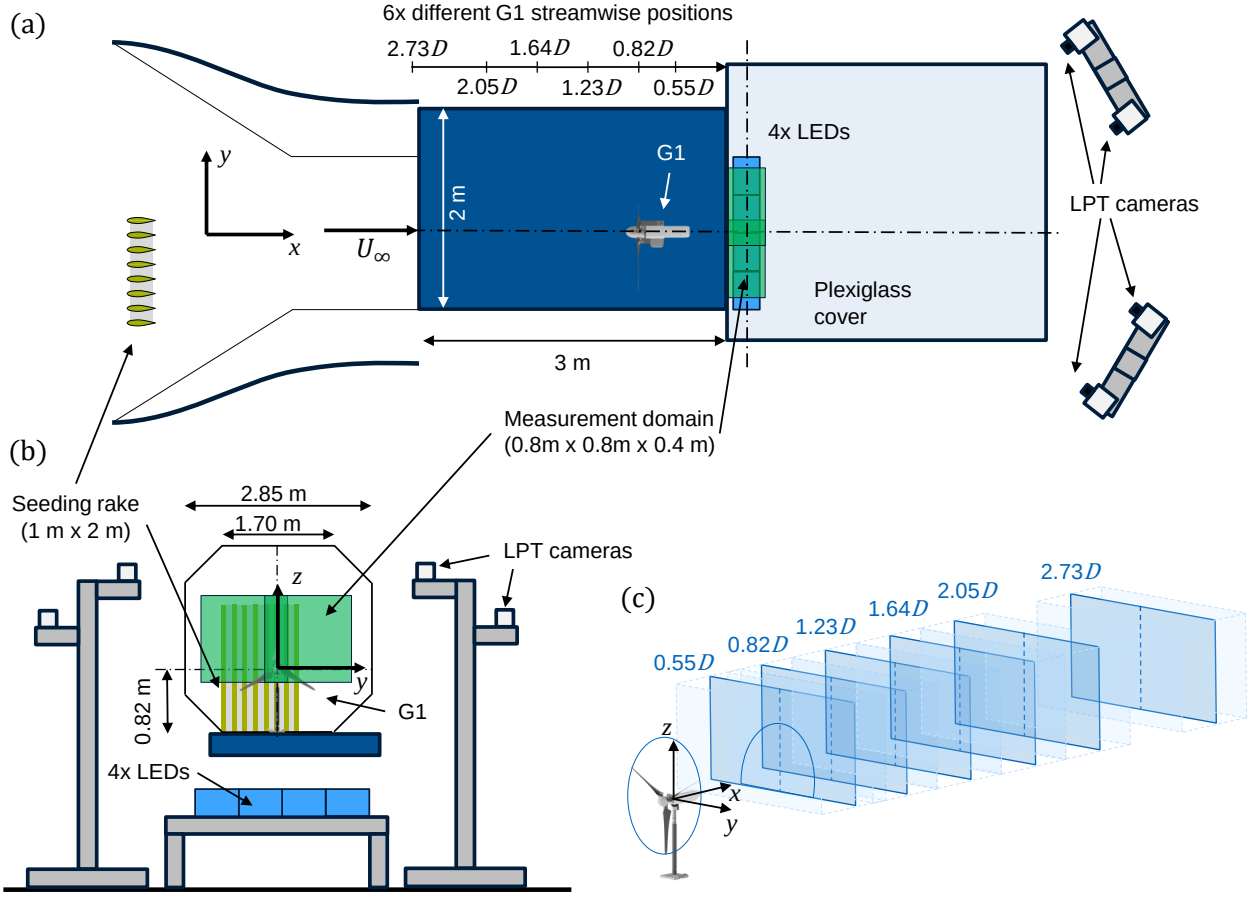


Figure 2. Experimental setup of wind tunnel campaign II. Top **(a)** and rear views **(b)** of the wind tunnel setup, and visualization of the six LPT measurement domains downstream **(c)**. The position of the measurement domain is fixed, while the G1 was moved in six positions to measure different streamwise portions of the wake, shown in panel c. The origin of the coordinate system coincides with the hub of the turbine and the rotor plane, but it is moved upstream in panel a for clarity.

https://doi.org/10.5194/wes-2026-214
Preprint. Discussion started: 19 November 2026
© Author(s) 2026. CC BY 4.0 License.



eawe european academy of wind energy
Open Access WIND ENERGY SCIENCE DISCUSSIONS

The wake was sampled at six downstream locations, namely $x/D = [0.55, 0.82, 1.23, 1.64, 2.05, 2.73]$ (corresponding to the center of the measurement volume), where $x = 0$ corresponds to the rotor center. As illustrated in Fig. 2, these measurement planes were obtained by translating the turbine relative to the fixed measurement volume. The procedure was then repeated after shifting the measurement volume laterally, allowing both halves of the wake to be reconstructed. The total measurement domain covers the whole near wake in the streamwise direction, from approximately $0.2 \lessapprox x/D \lessapprox 3$, extends for $-0.8 \lessapprox y/D \lessapprox 0.8$ in the lateral direction, and covers the upper portion of the wake at $z/D \gtrapprox -0.2$.

For each operating condition, 20 LPT acquisitions were performed with the cameras operating at 600 Hz, each over a predefined acquisition time, T_a. For the baseline and wake steering cases, T_a was set to 0.17 s, corresponding to 2.4 rotor revolutions. For the helix and helix+yaw cases, T_a was increased to 0.43 s, corresponding to one complete period of the helical wake motion, denoted by T_h.

LPT was performed using the Shake-The-Box algorithm (Schanz et al., 2016) implemented in the DaVis 10 software from LaVision GmbH. The Lagrangian particle tracks were then collected in Eulerian bins (Agüera et al., 2016) using a second-order polynomial regression for subsequent data processing. A bin with a side length of 64 voxels was used, corresponding to a 96 mm edge length per bin in physical space, with a 75% overlap and a minimum of 100 particles per bin for ensemble averaging. Hence, the resulting vector spacing was 24 mm.

To ensure phase consistency across the 20 repetitions, each acquisition was initiated by a trigger generated by the G1 control system. The primary trigger condition required the rotor azimuth, ψ, to reach 0° within a tolerance of $\pm 1^\circ$. This condition is sufficient for the baseline and wake steering cases, where the dominant source of wake asymmetry is the tip vortices. For the two cases employing helix control, an additional synchronization condition was imposed: simultaneously with the azimuth condition, the pitch angle of blade 1 had to coincide with the crest of its sinusoidal trajectory, i.e., $\beta_\mathrm{crest} = \beta_\mathrm{OPT} + A = 3.42^\circ$, within a tolerance of $\pm 0.05^\circ$.

3 Results

3.1 Wind tunnel campaign I: wind turbine cluster power

Figure 3 presents the power of two aligned G1s and their sum, in the boundary layer wind tunnel. The power values are shown for three control methods, and they are normalized to the baseline case, in which the front turbine operates at maximum efficiency. A bar showing the expected power is indicated by a black dashed outline. The expected value is obtained by assuming that the power gains from helix and wake steering are additive, i.e., by linearly superimposing the individual increases relative to the baseline.

Results indicate that WT_1 loses power as a result of its operation. The losses measured with wake steering are significantly larger than those resulting from pure helix. The power losses of wake steering + helix are in line with the expected value of $P/P_{\mathrm{Baseline},1}$ =79%. This implies that it is reasonable to assume that the power losses introduced by the variation of angle of attack of the helix can be superimposed on top the losses due to misaligned operation.

https://doi.org/10.5194/wes-2026-214
Preprint. Discussion started: 19 November 2026
© Author(s) 2026. CC BY 4.0 License.

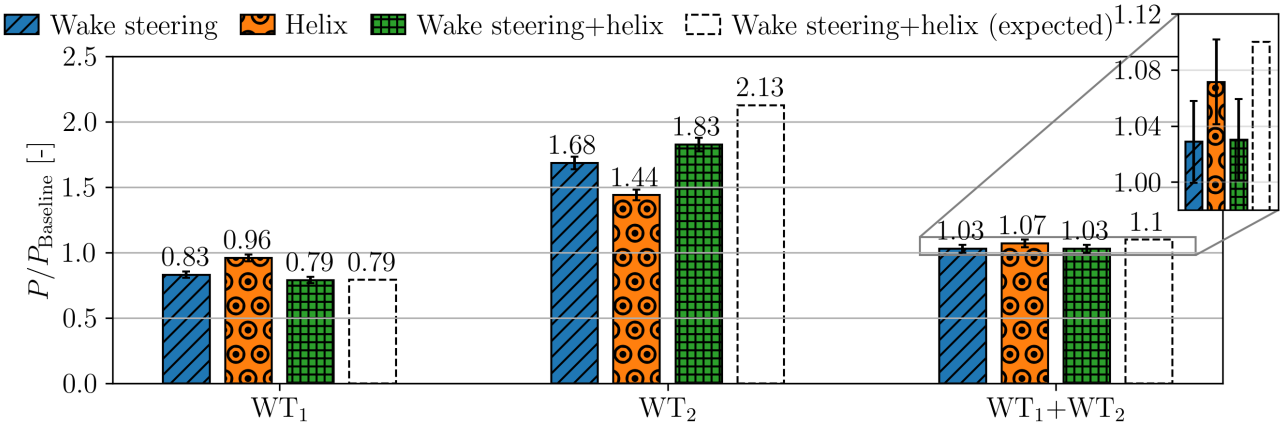


Figure 3. Local and collective power of two G1s in the boundary layer wind tunnel at Politecnico di Milano. The rotors are aligned at a distance of $5D$. Three control strategies are shown, and the data are normalized with the power measured with the baseline control method. WT_1 operates with a fixed rotational speed of 850 RPM, while WT_2 is controlled for maximum C_P. The expected performance of combined wake steering and helix, obtained by linearly summing the single techniques, is shown with a dashed black bar.

Contrary to WT_1, the power of WT_2 is significantly increased. The effectiveness of wake steering and helix is comparable, yet their combination does not result in a larger power gain. The results are remarkable, since the expected power boost on WT_2 $P/P_{\text{Baseline},2}$ is 2.13, while the measured one is only 1.83. As a result, the combination of wake steering and helix does not yield any additional power benefit to the wind farm compared to the single techniques. Similar results are also obtained with variable Ω on WT_1, and are reported in Appendix A.

In the next section, we examine the wake measurements to identify the cause of the poor performance of the combined approach.

3.2 Wind tunnel campaign II: wake characterization

3.2.1 Temporal evolution of the wake

Figures 4, 5, 6 and 7 present the temporal evolution of vorticity magnitude $|\omega|$ on a horizontal plane at hub height, throughout one revolution of the rotor. Figure 4 corresponds to the baseline case, Fig. 5 to the wake steering experiment, Fig. 6 to the pure helix control case, and Fig. 7 to the combined helix and wake steering case. In the cases with helix, the time evolution is reported throughout one helix period T_h. while in the other cases, a full rotor cycle T_r is shown. The plots are obtained by stitching together the six measurement domains, taking advantage of the acquisition trigger used to synchronize the LPT system with the G1 turbine, as explained in Sect. 2.2. The stitching of the six measurement domains may introduce artificial vorticity peaks at the domain interfaces. The locations of these artefacts are indicated in the captions of the corresponding figures.

https://doi.org/10.5194/wes-2026-214
Preprint. Discussion started: 19 November 2026
© Author(s) 2026. CC BY 4.0 License.

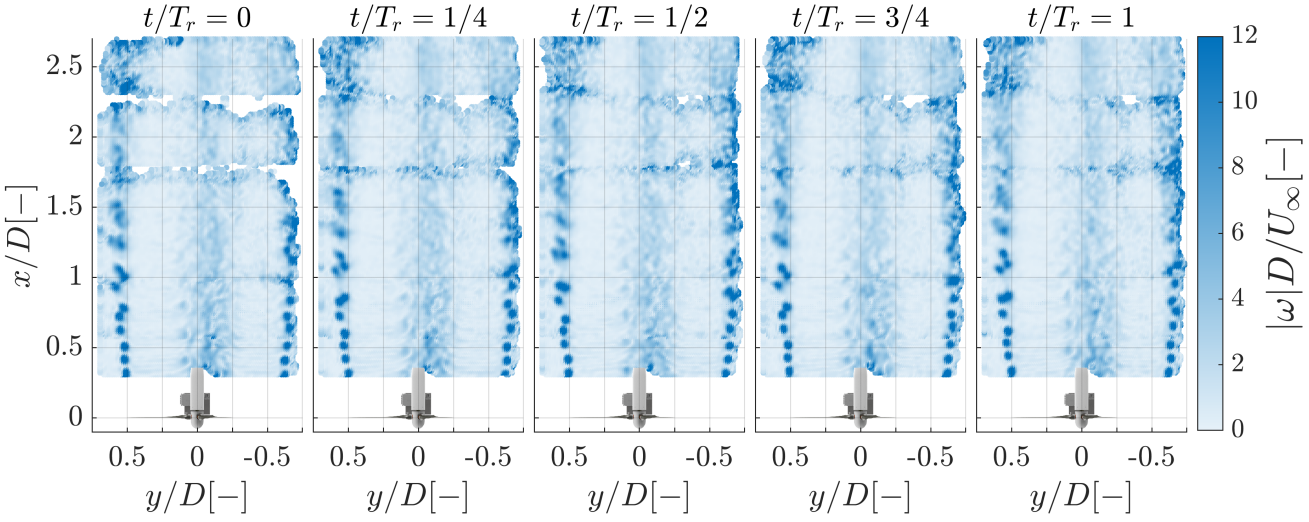


Figure 4. Normalized instantaneous fields of vorticity magnitude $|\omega|$ on a xy plane at hub height. Lagrangian particle tracking data for the baseline control case. From left to right, each subplot corresponds to an increasing time instant t, defined in the titles as a fraction of the rotor revolution period $T_r = 60/\Omega_R$. Artificial vorticity peaks may occur at the domain interfaces around $x/D \approx 1.7$ and $x/D \approx 2.3$. Video link: https://youtu.be/j5RloNF93w8

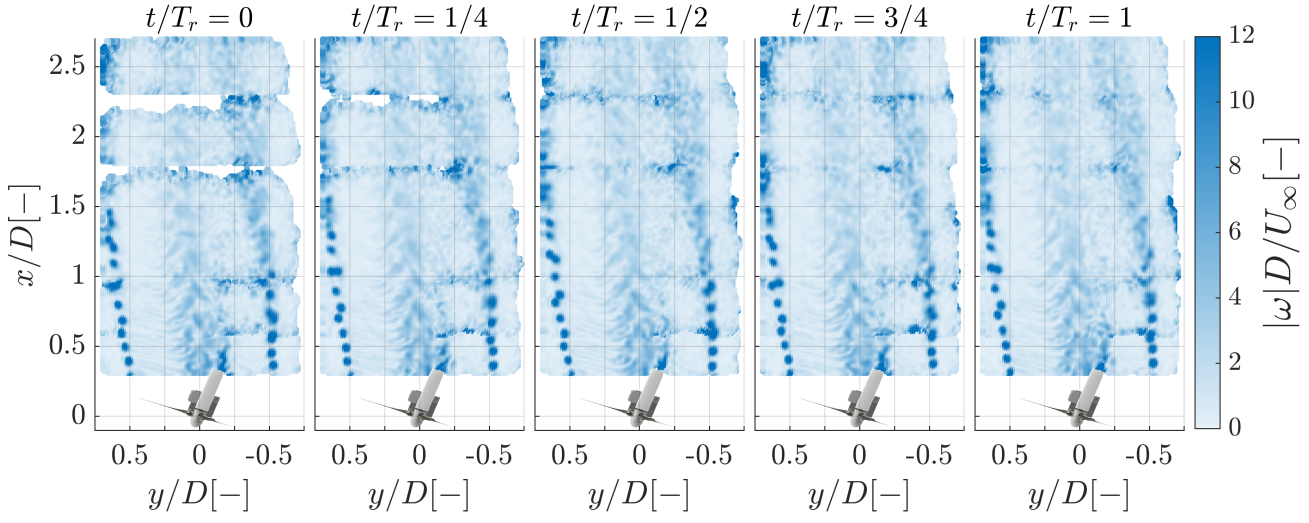


Figure 5. Normalized instantaneous fields of vorticity magnitude $|\omega|$ on a xy plane at hub height. Lagrangian particle tracking data for the wake steering control case. From left to right, each subplot corresponds to an increasing time instant t, defined in the titles as a fraction of the rotor revolution period $T_r = 60/\Omega_R$. Artificial vorticity peaks may occur at the domain interfaces around $x/D \approx 1.7$ and $x/D \approx 2.3$. Video link: https://youtu.be/j5RloNF93w8

https://doi.org/10.5194/wes-2026-214
Preprint. Discussion started: 19 November 2026
© Author(s) 2026. CC BY 4.0 License.

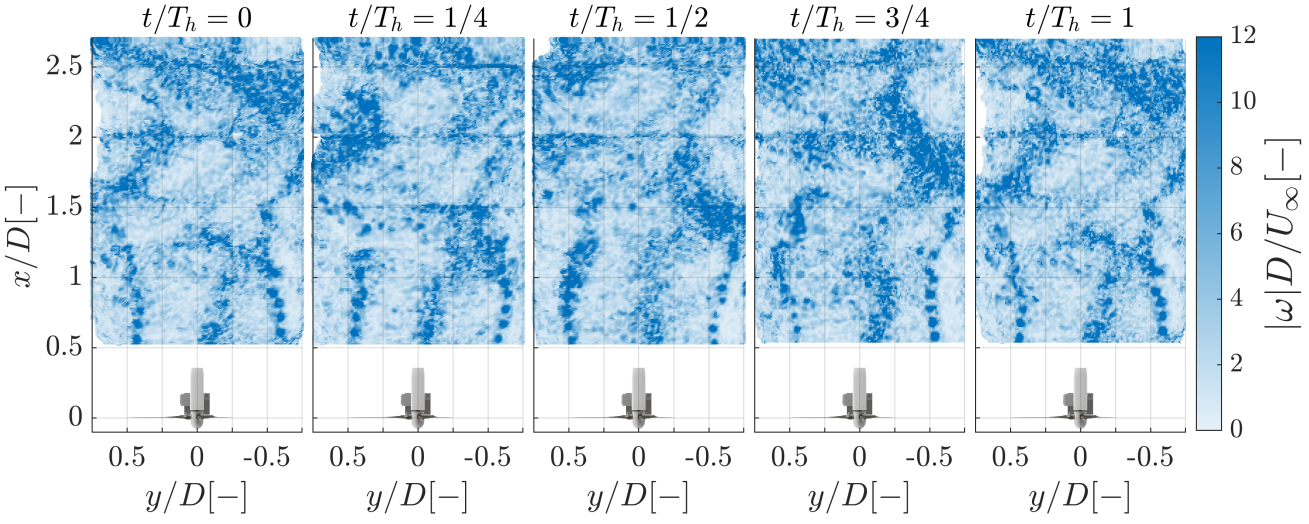


Figure 6. Normalized instantaneous fields of vorticity magnitude $|\omega|$ on a xy plane at hub height. Lagrangian particle tracking data for the helix control case. From left to right, each subplot corresponds to an increasing time instant t, defined in the titles as a fraction of the period of the helix T_h. Artificial vorticity peaks may occur at the domain interfaces around $x/D \approx 1.5$, $x/D \approx 2$, and $x/D \approx 2.5$. Video link: https://youtu.be/j5RloNF93w8

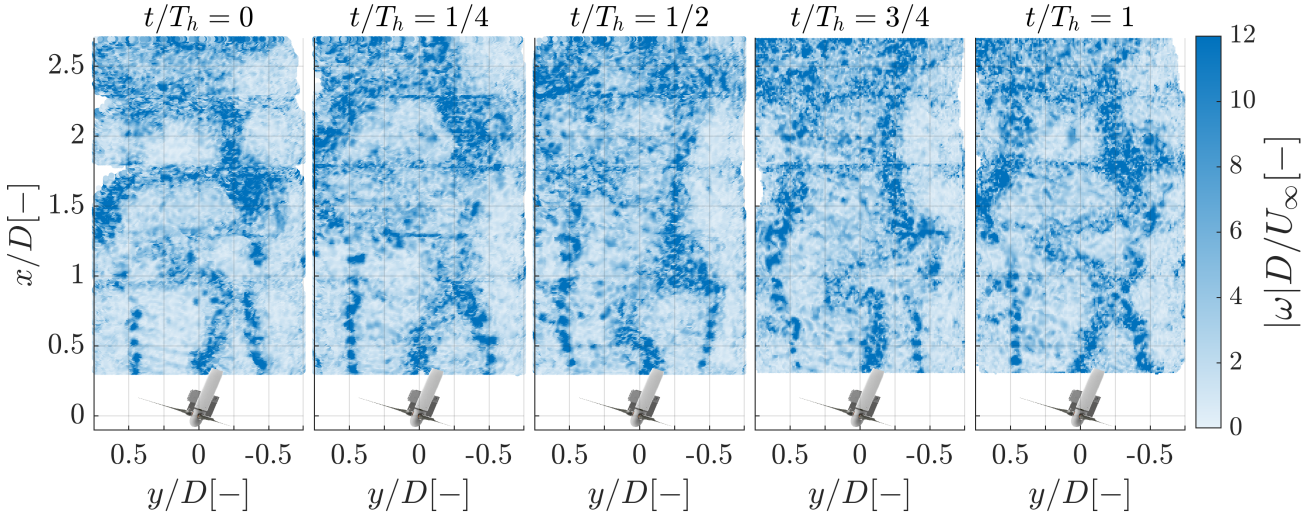


Figure 7. Normalized instantaneous fields of vorticity magnitude $|\omega|$ on a xy plane at hub height. Lagrangian particle tracking data for the combined helix and wake steering control case. From left to right, each subplot corresponds to an increasing time instant t, defined in the titles as a fraction of the period of the helix T_h. Artificial vorticity peaks may occur at the domain interfaces around $x/D \approx 1$, $x/D \approx 1.3$, $x/D \approx 1.8$, and $x/D \approx 2.2$. Video link: https://youtu.be/j5RloNF93w8

https://doi.org/10.5194/wes-2026-214
Preprint. Discussion started: 19 November 2026
© Author(s) 2026. CC BY 4.0 License.



eawe european academy of wind energy
Open Access WIND ENERGY SCIENCE DISCUSSIONS

The plots clearly visualize the tip vortices traveling downstream at $|y|/D \geq 0.5$. In cases without helix, tip vortices begin to interact at $x/D \approx 0.6$ and eventually lose their coherence at $x/D > 1.5$. For pure wake steering in Fig. 5, the wake is clearly displaced laterally due to yaw misalignment. In the pure helix case in Fig. 6, the wake exhibits a clear and regular meandering path, with a wavelength of approximately $1D$. Tip vortices lose their coherence earlier than in the baseline and wake steering cases, at $x/D \approx 1.2D$. In the combined helix and wake steering scenario shown in Fig. 7, the sinusoidal wake trajectory is less apparent. This may indicate a reduction in the wake meandering amplitude, although it could also result from the kidney-shaped wake cross-section induced by yaw misalignment (Bartl et al., 2018), which makes the meandering motion more difficult to discern from the top-view visualization. A lateral displacement of the meandering wake towards positive y can be seen when comparing with the pure helix case in Fig. 6. However, it is also less evident than in the pure wake steering case in Fig. 5.

These qualitative observations suggest that the effectiveness of displacement and meandering (and thus mixing) of wake steering and helix, respectively, is somewhat reduced when both techniques are applied simultaneously. This interpretation is consistent with the quantitative power measurements from the wind tunnel campaign I presented in Sect. 3.1.

3.2.2 Wake mixing

Next, we determine the effectiveness of mixing by introducing the flux of mean kinetic energy due to shear stress

$$\Phi_{xy} = -\overline{u'v'}\overline{u},$$

considering the horizontal xy plane at $z = z_{\mathrm{hub}}$. Φ_{xy} arises from the mean kinetic energy budget equation. Under boundary-layer-type approximations, this term provides a quantitative measure of the entrainment of free-stream high-momentum flow into the wake (Cal et al., 2010; van der Hoek et al., 2024). Figure 8 presents Φ_{xy} for the four control cases, normalized with the free-stream velocity.

The plots clearly show that activating the helix results in relatively high values of Φ_{xy}, indicating enhanced exchange between the high-momentum flow outside the wake and the wake itself. However, a qualitative comparison between the helix-only case and the combined helix and wake steering cases, shown in panels c and d, reveals that Φ_{xy} is slightly lower when both control strategies are applied simultaneously.

3.2.3 Tracking of vortex interactions

Next, we analyze the LPT data on a yz plane parallel to the rotor, at the farthest measurement domain of $x/D = 2.73$. The goal of this analysis is to determine the flow field characterizing the wake under the four different control methods.

Figure 9 presents the mean planar flow streamlines at $x/D = 2.73$ for baseline and wake steering. The normalized lateral velocity field $\overline{v}$ is also shown, alongside with vortex centers, which are identified using the Γ_1 algorithm by Graftieaux et al. (2001). The Γ_1 criterion was selected because it provides a robust and computationally simple identification of the vortex centers directly from the measured velocity field.

The baseline case in Fig. 9a is characterized by one main vortex, centered approximately at the rotor center. This coincides with the well-known counter-rotation of the wake with respect to the rotor (Hansen, 2015). At the same time, it is also not

https://doi.org/10.5194/wes-2026-214
Preprint. Discussion started: 19 November 2026
© Author(s) 2026. CC BY 4.0 License.

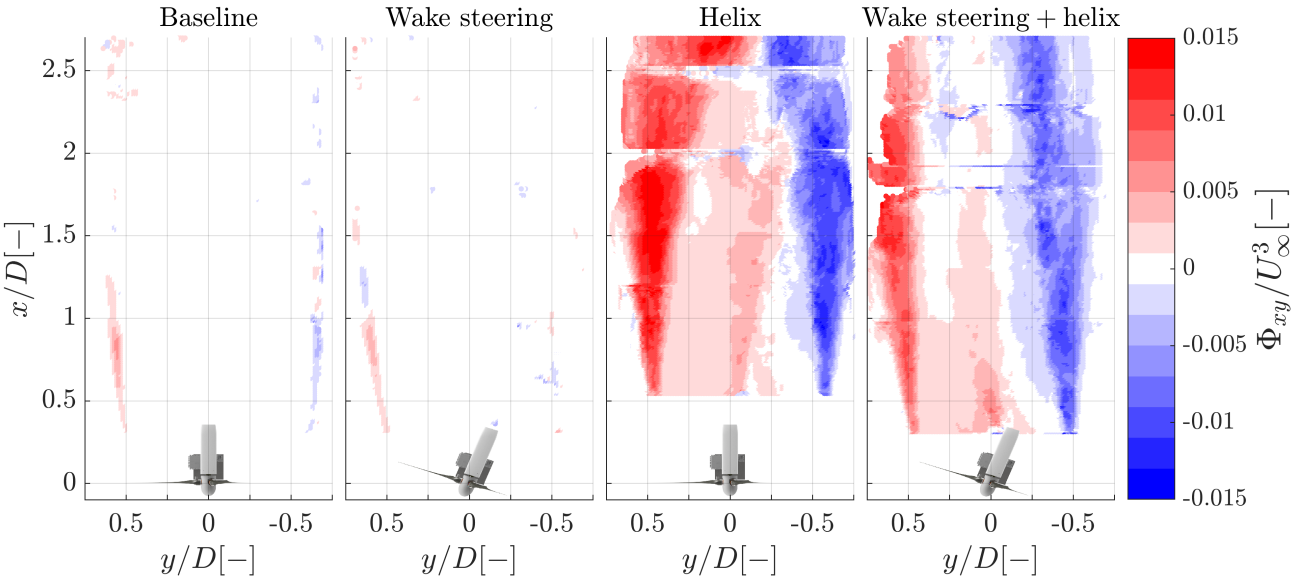


Figure 8. Fluxes of mean kinetic energy due to shear stress Φ_{xy}, computed on a horizontal xy plane at $z = z_{\mathrm{hub}}$ for baseline, wake steering, helix, combined helix and wake steering control cases. The plots are obtained by stitching together the six LPT measurement domains along the streamwise direction.

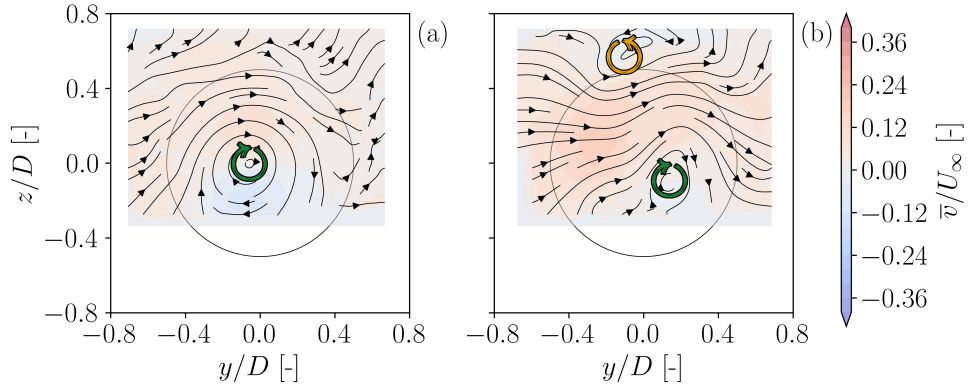


Figure 9. Mean lateral velocity field $\overline{v}$ for baseline **(a)** and steering **(b)** on a plane parallel to the rotor at $x/D = 2.73D$ obtained with LPT. View of an observer looking upstream. $\overline{v}$ is normalized with the free-stream velocity U_∞. Streamlines are overlaid on the contour with solid black lines and arrows. Vortex centers are detected using the Γ_1 algorithm by Graftieaux et al. (2001) and shown with clockwise and counterclockwise arrow markers.

https://doi.org/10.5194/wes-2026-214
Preprint. Discussion started: 19 November 2026
© Author(s) 2026. CC BY 4.0 License.



eawe european academy of wind energy
Open Access WIND ENERGY SCIENCE DISCUSSIONS

surprising to observe two counter-rotating vortices for the wake steering case in Fig. 9b. This pair of vortices is, in fact, typical of the wake of a misaligned rotor and has often been reported in the literature (Bastankhah and Porté-Agel, 2016; Branlard and Gaunaa, 2016; Howland et al., 2016; Shapiro et al., 2020).

Next, we present the same plots, but this time for the helix (Fig. 10) and the combination of helix and wake steering (Fig. 11). Due to the unsteady behavior of the wake in this case, each figure includes 12 subplots that show the instantaneous flow fields at progressively increasing fractions of the helix period T_{helix}. This allows tracking the evolution of the wake throughout a full revolution of its helical motion.

In several instances, the dominant vortical structure lay partially or fully outside the measurement domain, and no local extremum satisfying the Γ_1 threshold could be identified. For these cases, the vortex location was instead estimated by fitting an ideal point-vortex model,

$$v(y,z) = -\frac{\Gamma}{2\pi}\frac{z-z_0}{(y-y_0)^2+(z-z_0)^2}, \qquad w(y,z) = \frac{\Gamma}{2\pi}\frac{y-y_0}{(y-y_0)^2+(z-z_0)^2}, \tag{1}$$

to the measured in-plane velocity field (v,w), where (y_0,z_0) and Γ denote the vortex center and circulation, respectively. The three parameters were obtained via nonlinear least-squares minimization of the residual between the modeled and measured velocity components, seeded from the vortex position of the previous time step. The optimization was constrained to a limited search region near the measurement boundary, selected according to the expected trajectory of the vortex during its helical motion. Furthermore, the solution is constrained to $\Gamma > 0$, consistent with the counterclockwise rotation expected for this vortex. Positions obtained through this fitting procedure are hereafter referred to as "ghost" vortex centers and are distinguished from directly detected ones in the figures.

In the helix case in Fig. 10, a strong counterclockwise vortex is clearly visible in the first time instant $t = 1/12T_{\mathrm{helix}}$, at $(y,z) \approx (0.2D, 0.5D)$. As time progresses, this vortex moves along a counterclockwise circular trajectory, approximately centered at $(y,z) = (0,0)$ and with a radius of approximately $0.5D$. For $5/12 \leq t/T_{\mathrm{helix}} \leq 2/3$, this coherent structure is not visible, since it exits the measurement domain for $z/D < 0.2$. Nevertheless, its presence remains evident through the velocity field it induces within the measurement region. This vortex is the "outer vortex" described by Gutknecht et al. (2025a). Two clockwise vortices are also shortly visible for $7/12 \leq t/T_{\mathrm{helix}} \leq 2/3$, which seem to be induced by the main vortex and are likely "secondary vortices" that have also been observed numerically by Gutknecht et al. (2025a).

Results are rather different for the combined helix and wake steering in Fig. 11. Also here, a strong counterclockwise vortex is visible in the first time instant. However, its anticlockwise rotation appears to be significantly slower than that of a pure helix. In fact, although the initial vortex position is similar, at the (exemplary) time instant $t = 1/3T_{\mathrm{helix}}$, it is centered at $(y,z) \approx (-0.4D, 0.4D)$ for helix + wake steering, while for pure helix its center is at $(y,z) \approx (-0.7D, -0.1D)$. In particular, the vortex appears to weaken as it approaches negative z values. Shortly after reaching $z/D \approx 0$, it is lost at $t = 7/12T_{\mathrm{helix}}$, but it is visible immediately afterward at $t = 2/3T_{\mathrm{helix}}$. Its vertical position is again $z/D \approx 0$, but the lateral one is mirrored compared to the last detected y position. For $t \geq 2/3T_{\mathrm{helix}}$, the vortex resumes its rotation along the counterclockwise trajectory and gains strength.

https://doi.org/10.5194/wes-2026-214
Preprint. Discussion started: 19 November 2026
© Author(s) 2026. CC BY 4.0 License.

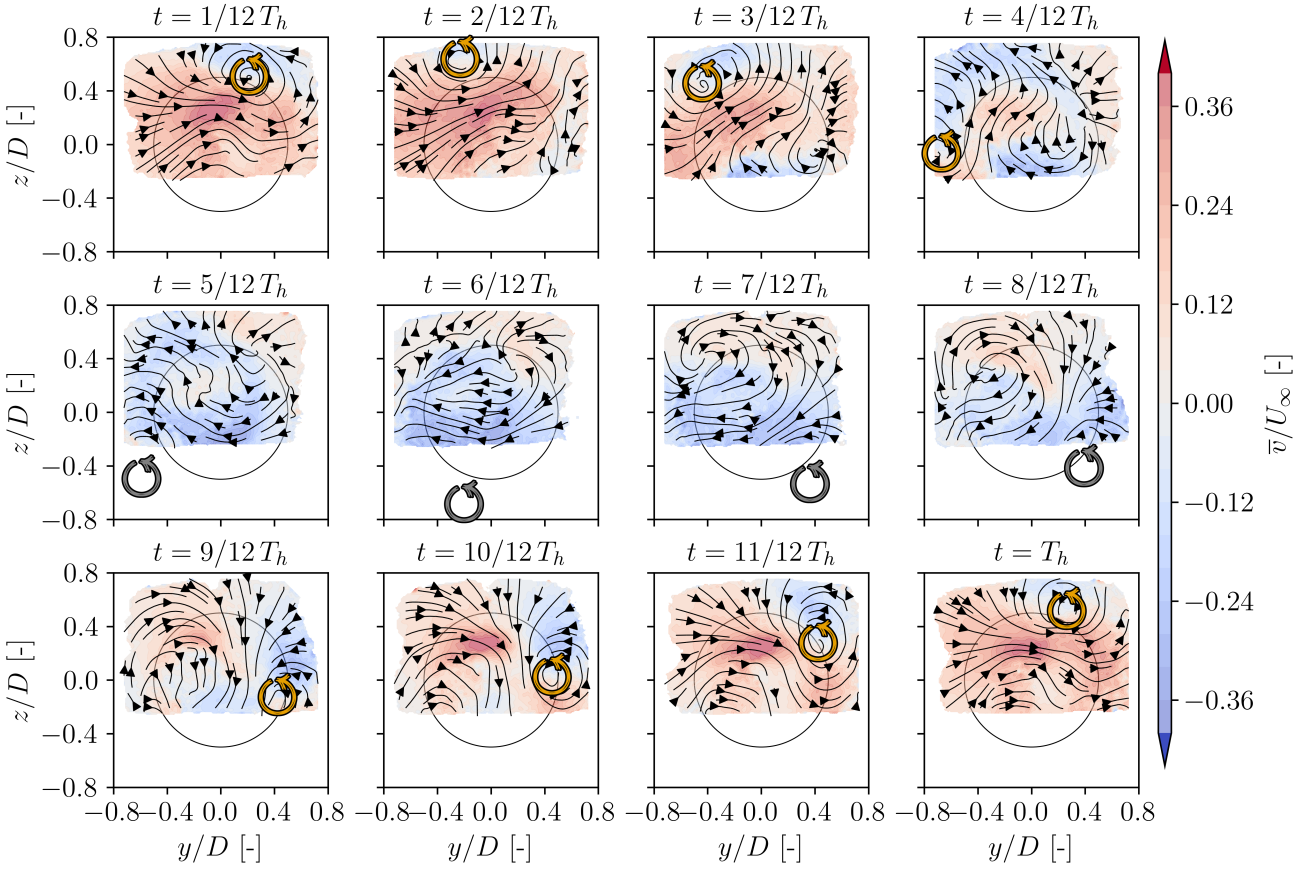


Figure 10. Instantaneous lateral velocity fields for the helix case on a plane parallel to the rotor at $x/D = 2.73D$ obtained with LPT. View of an observer looking upstream. Different times t are reported as a fraction of the period of the helix, T_{helix}. The streamlines are overlaid on top of the contour with solid black lines featuring arrows. Vortex centers are detected using the Γ_1 algorithm by Graftieaux et al. (2001) and shown with clockwise and counterclockwise arrow markers. When the main counterclockwise-rotating vortex was not detected within the field of view, its location (outside the measurement domain) was estimated by fitting an ideal point-vortex model to the surrounding velocity field, and it is shown in gray. The rotor perimeter is also plotted as a reference. Video link: https://youtu.be/BgF-UREulio

https://doi.org/10.5194/wes-2026-214
Preprint. Discussion started: 19 November 2026
© Author(s) 2026. CC BY 4.0 License.

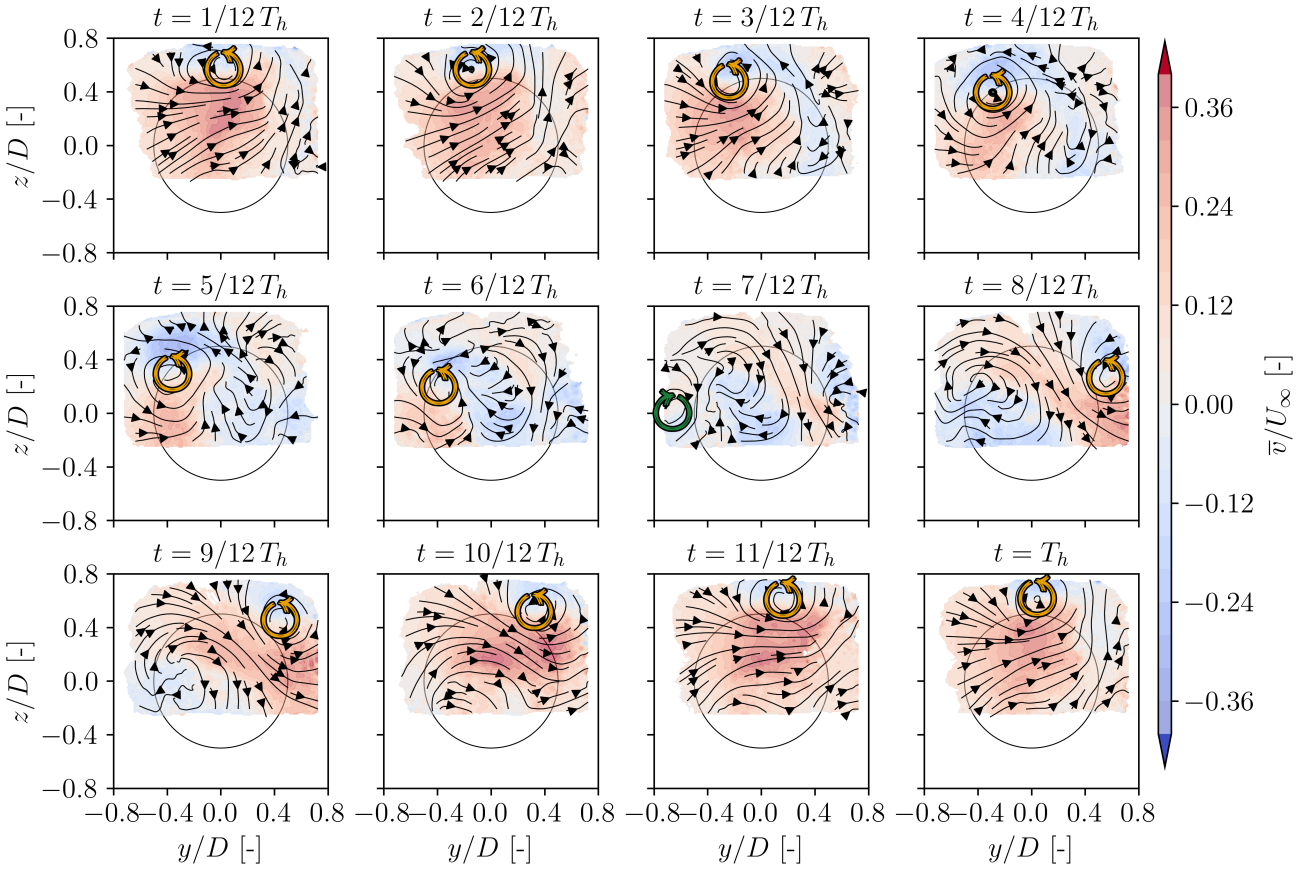


Figure 11. Instantaneous lateral velocity fields for the combination of helix and steering on a plane parallel to the rotor at $x/D = 2.73D$ obtained with LPT. View of an observer looking upstream. Different times t are reported as a fraction of the period of the helix, T_{helix}. The streamlines are overlaid on top of the contour with solid black lines featuring arrows. Vortex centers are detected using the Γ_1 algorithm by Graftieaux et al. (2001) and shown with clockwise and counterclockwise arrow markers. Video link: https://youtu.be/BgF-UREulio

https://doi.org/10.5194/wes-2026-214
Preprint. Discussion started: 19 November 2026
© Author(s) 2026. CC BY 4.0 License.



eawe european academy of wind energy
Open Access WIND ENERGY SCIENCE DISCUSSIONS

The lateral velocity field provides further evidence of the altered wake dynamics. In the pure helix case (Fig. 10), a well-organized alternating pattern of positive and negative lateral velocity is observed throughout the helix period. Excluding the transition phases, during which the flow is predominantly directed upward or downward, the flow is directed predominantly toward positive y for $0 \leq t/T_{\text{helix}} \leq 1/3$ and $3/4 \leq t/T_{\text{helix}} \leq 1$, whereas it is directed toward negative y for approximately $1/3 \leq t/T_{\text{helix}} \leq 3/4$. In the combined helix and wake steering case, this alternating pattern is much less pronounced. In particular, during the interval $5/12 \leq t/T_{\text{helix}} \leq 7/12$, where a predominantly negative lateral velocity would be expected based on the pure helix case, the flow instead exhibits a mixed pattern with locally positive and negative lateral velocities. This observation is consistent with the weakening of the orbiting vortex for $z < 0$ and further supports the hypothesis that the yaw-induced vortices disrupt the coherent lateral motion generated by helix control.

Overall, the counterclockwise vortex seems to perform a full rotation for pure helix, while it seems to follow only half of the trajectory (for $z > 0$) when helix and wake steering are combined. Figure 12 illustrates the three-dimensional temporal trajectories of the outer vortex.

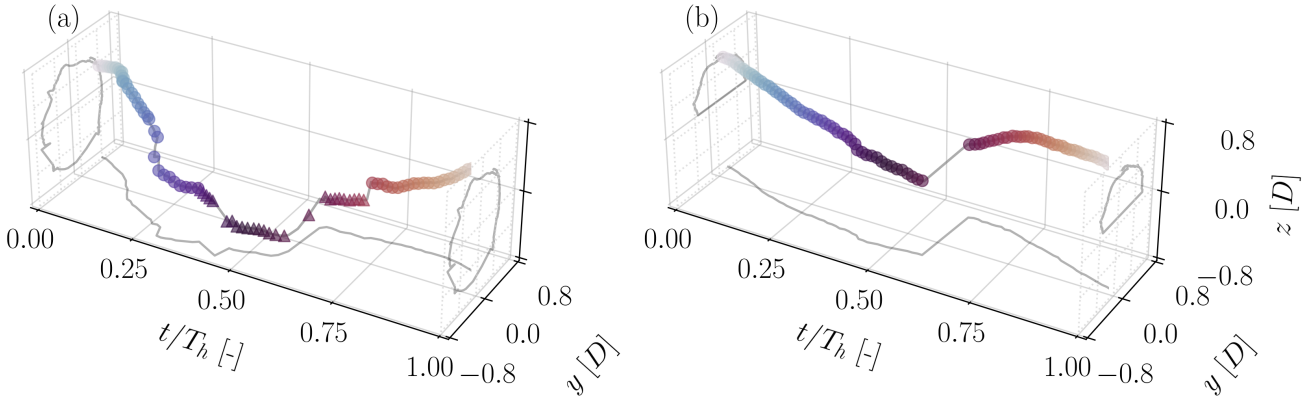


Figure 12. Three-dimensional trajectory lines and temporal evolution of the main outer vortex position over a full helix period T_{h} for: the pure helix case **(a)**, and the combination of helix motion and yaw-based wake steering **(b)**. Data from a yz plane at $x/D = 2.73$. Circles (•) denote standard vortex centers directly resolved via the Γ_1 algorithm, while triangles (▲) signify "ghost" vortex centers reconstructed outside the measurement boundary using the non-linear least-squares ideal point-vortex model fitting. Markers are color-coded by the normalized time progress t/T_{h}. Grey lines indicate the 2D spatial projections of the trajectory onto the background boundary planes.

In the pure helix configuration (Fig. 12a), the vortex successfully completes a full circular revolution, whereas the combined steering case (Fig. 12b) shows the vortex trajectory confined almost exclusively to the upper half-plane ($z/D > 0$).

This phenomenon can be explained by the counter-rotating vortices introduced with yaw misalignment, which we have shown in Fig. 9b. In particular, the "upper vortex" at $z > 0$ rotates counterclockwise, while the "lower" one at $z < 0$ rotates clockwise. If we assume that the locations of the counter-rotating vortices due to yawed operation are fixed in space, while the helical vortex moves throughout a period of the helix, then it is reasonable that a phenomenon of amplification and cancellation

https://doi.org/10.5194/wes-2026-214
Preprint. Discussion started: 19 November 2026
© Author(s) 2026. CC BY 4.0 License.

takes place. In fact, the counterclockwise vortex of the helix is amplified by the "upper vortex" for $z > 0$. However, it is also weakened by the "lower vortex" for $z < 0$. As a result, its orbiting path is perturbed, and its effectiveness in entraining high velocity fluid into the wake is reduced. Similarly, the two counter-rotating vortices induced by yaw misalignment are less prominent, and this affects the lateral wake displacement.

To provide quantitative support for this amplification–cancellation mechanism, we computed the circulation of the outer vortex directly from the measured velocity field, rather than relying on a model-based estimate. At each time instant, the vortex center is located using the Γ_1 algorithm by Graftieaux et al. (2001), and the circulation is obtained as a line integral of the measured velocity along a circle of fixed radius $r = 0.1D$ centered on that point, i.e.,

$$\Gamma = \oint_{C(r)} \mathbf{u} \cdot \mathrm{d}\mathbf{l}. \tag{2}$$

The same expression is used for the helix and the combined helix and wake-steering cases so that any difference in Γ reflects a genuine difference in vortex strength rather than a difference in how it was measured. The integration radius r is chosen as the smallest radius that consistently encloses the identified vortex core across all considered frames. Figure 13 shows the resulting normalized circulation $\Gamma^* = \Gamma/(U_\infty D)$ over one helix period (panel a), together with the corresponding trajectory of the vortex center in the yz-plane (panel b).

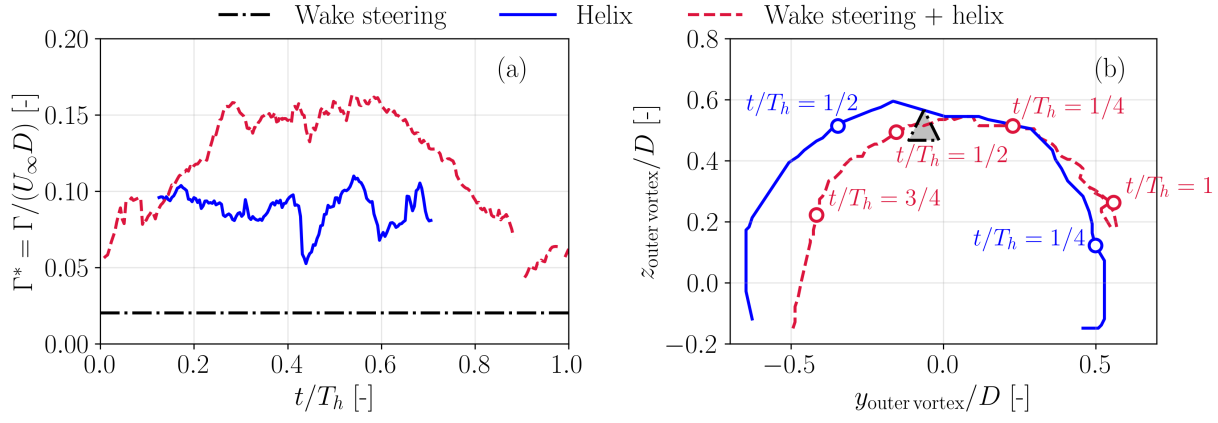


Figure 13. Normalized circulation $\Gamma^* = \Gamma/(U_\infty D)$ of the outer vortex over one helix period T_h at $x/D = 1.64$, computed as a velocity line integral on a circle of radius $r = 0.1D$ around the vortex center located via the Γ_1 algorithm by Graftieaux et al. (2001), for helix (blue, solid) and the combination of helix and wake steering (red, dashed) **(a)**. The black dotted line denotes the time-averaged circulation of the steady counter-rotating vortex pair generated by wake steering alone. Corresponding trajectory of the outer vortex center in the yz-plane for helix (blue) and helix combined with wake steering (red) **(b)**. Open circles mark the vortex position at given values of t/T_h. The grey triangle marks the time-averaged position of the wake-steering-only vortex center, shown for reference.

The circulation history in panel a shows that, for the helix case, Γ^* remains nearly constant over the portion of the cycle captured within the measurement domain. Data are unavailable for $0.15 < t/T_h < 0.7$, as the outer vortex moves outside

https://doi.org/10.5194/wes-2026-214
Preprint. Discussion started: 19 November 2026
© Author(s) 2026. CC BY 4.0 License.



eawe european academy of wind energy
Open Access WIND ENERGY SCIENCE DISCUSSIONS

the field of view. In contrast, when the helix is combined with wake steering, Γ^* exhibits a pronounced maximum around $t/T_h \approx 0.5$.

The corresponding vortex trajectories in panel b indicate that, at $t/T_h \approx 0.5$, the outer helix vortex passes closest to the counterclockwise vortex generated by wake steering. This temporal coincidence with the peak in Γ^* supports the interpretation that the two vortices undergo constructive superposition, leading to a temporary increase in the measured circulation. As the helix vortex subsequently moves away from the wake-steering vortex toward lower z-positions, the spatial overlap between the two structures decreases, and the measured circulation returns to values comparable – if not lower – to those of the helix case alone. The plots of the trajectory also show that the vortex travels significantly faster in the case of pure helix control. This is particularly visible when comparing the positions at the consecutive times $t/T_h = 1/4$ and $t/T_h = 1/2$.

At first sight, the local amplification and weakening of the helix-vortex circulation might suggest that the effects should compensate over one complete helix cycle. However, such a cancellation does not happen because the two control effects do not contribute symmetrically to the wake dynamics. For wake steering, the lateral wake displacement relies on the coherent action of the counter-rotating vortex pair, which is responsible for creating a lateral jet of air that displaces the wake sideways. The interaction with the helix vortex, therefore, breaks the symmetry of this pair and weakens the lateral jet; strengthening of the interacting vortex during part of the cycle does not compensate for this loss. For helix control, the situation is more complex: although the circulation of the helix vortex is temporarily amplified when it approaches the steering vortex, the interaction also substantially alters its trajectory. The resulting vortex motion is effectively smaller than the approximately circular orbit responsible for enhanced mixing in the helix-only case. It is reasonable to assume that this should result in a lower mixing capability. Thus, the interaction does not simply cancel over a helix cycle; instead, it modifies the coherent vortex structures through which both control strategies act.

The experimental results presented above support the hypothesis that the altered trajectory of the helix vortex results from its interaction with the counter-rotating vortex pair generated by wake steering. For the negative yaw angle considered experimentally, this interaction favors the persistence of the counterclockwise-rotating helix vortex in the upper half-plane, while its motion toward the lower half-plane is inhibited. If this interpretation is correct, reversing the yaw direction should reverse the asymmetry, causing the helix vortex to preferentially persist in the lower half-plane. Since the opposite yaw configuration was not investigated experimentally, LES-ALM simulations are used to test this prediction.

3.2.4 Numerical verification of the proposed vortex interactions

LES-ALM were performed using AMR-Wind v3.8 (Kuhn et al., 2025), an incompressible flow solver coupled with OpenFAST v4.1 (NREL, 2023). The simulations reproduce the wind-tunnel configuration for the experimentally investigated negative yaw angle and, additionally, consider the opposite yaw direction. The latter configuration was not investigated experimentally and is used to test whether reversing the yaw-induced vortex pair also reverses the preferential half-plane of the helix-vortex trajectory.

The computational domain extends $19.2 \times 7 \times 7$ D in the streamwise, lateral, and vertical directions, with four nested cubic refinement regions covering the rotor and its wake. An additional annular refinement region is applied in the vicinity of the rotor. The resulting mesh contains approximately 91 million cells.

https://doi.org/10.5194/wes-2026-214
Preprint. Discussion started: 19 November 2026
© Author(s) 2026. CC BY 4.0 License.



eawe european academy of wind energy
Open Access WIND ENERGY SCIENCE DISCUSSIONS

The low turbulence intensity of the wind-tunnel inflow was reproduced using the synthetic turbulence method of Troldborg et al. (2014). Turbulent fluctuations generated from a Kaimal spectrum (Jonkman, 2016) were introduced $3.75D$ upstream of the rotor, with a target turbulence intensity of 2% at hub height and a turbulence length scale of $0.05D$. The subgrid-scale stresses were modeled using the standard Smagorinsky model with $C_s = 0.17$ (Sagaut, 2006). The main numerical parameters are summarized in Table 3.

Table 3. Summary of the numerical setup used for the LES-ALM simulations.

Domain size	$19.2 \times 7 \times 7$ D (length $\times$ width $\times$ height)
Total cells	≈ 91 million
Mesh size at the rotor	$\Delta x = 0.01D$
Finest mesh size	$0.005D$ (annular refinement)
Time step	0.2 ms
ALM Gaussian kernel	$\epsilon = 1.5\Delta x$
Actuator points per blade	60
Subgrid-scale model	Smagorinsky, $C_s = 0.17$

Figures 14 and 15 present the planar velocity field at $x/D = 3$ for the combination of helix with negative and positive yaw angles, respectively (similarly to Sect. 3.2.3). In each figure, 12 subplots show the temporal evolution of the flow field over one period of the helix, T_h. Also here, the Γ_1 algorithm by Graftieaux et al. (2001) is used to locate the dominant vortical structures. Results for pure helix are included in Appendix B.

The numerical results for the negative yaw case in Fig. 14 are consistent with the experimental observations in Fig. 11. The outer vortex generated by helix control preferentially orbits in the upper half-plane, $z > 0$. When the yaw angle is reversed to $\gamma = +20°$, however, Fig. 15 shows that the same vortex preferentially moves through the lower half-plane, $z < 0$. This reversal is consistent with the proposed constructive and destructive interaction mechanism. For $\gamma = +20°$, the wake is deflected toward negative y. For an observer looking upstream, the corresponding wake-steering vortex pair consists of a clockwise-rotating vortex in the lower half-plane and a counterclockwise-rotating vortex in the upper half-plane. The clockwise outer vortex generated by the helix is therefore reinforced in the lower half-plane and weakened in the upper half-plane. Reversing the yaw angle switches the signs of the wake-steering vortices and consequently reverses this preferential interaction, consistently with the experimentally observed behavior for $\gamma = -20°$.

The analyses above consider only clockwise helix excitation (i.e., $k < 1$). The proposed interaction mechanism also leads to a further prediction: reversing the direction of the helix excitation (i.e., $k > 1$) should reverse the sign of the outer helix vortex and, consequently, the half-plane in which it preferentially persists. This would produce an effect analogous to reversing the yaw angle. Such a reversal is expected because the sign of the outer vortex generated by helix control depends on the direction of the helix excitation (Gutknecht et al., 2025a). Thus, the proposed mechanism predicts that reversing either the yaw direction or the helix excitation direction should reverse the preferential half-plane of the orbiting helix vortex. In other words, since the

https://doi.org/10.5194/wes-2026-214
Preprint. Discussion started: 19 November 2026
© Author(s) 2026. CC BY 4.0 License.

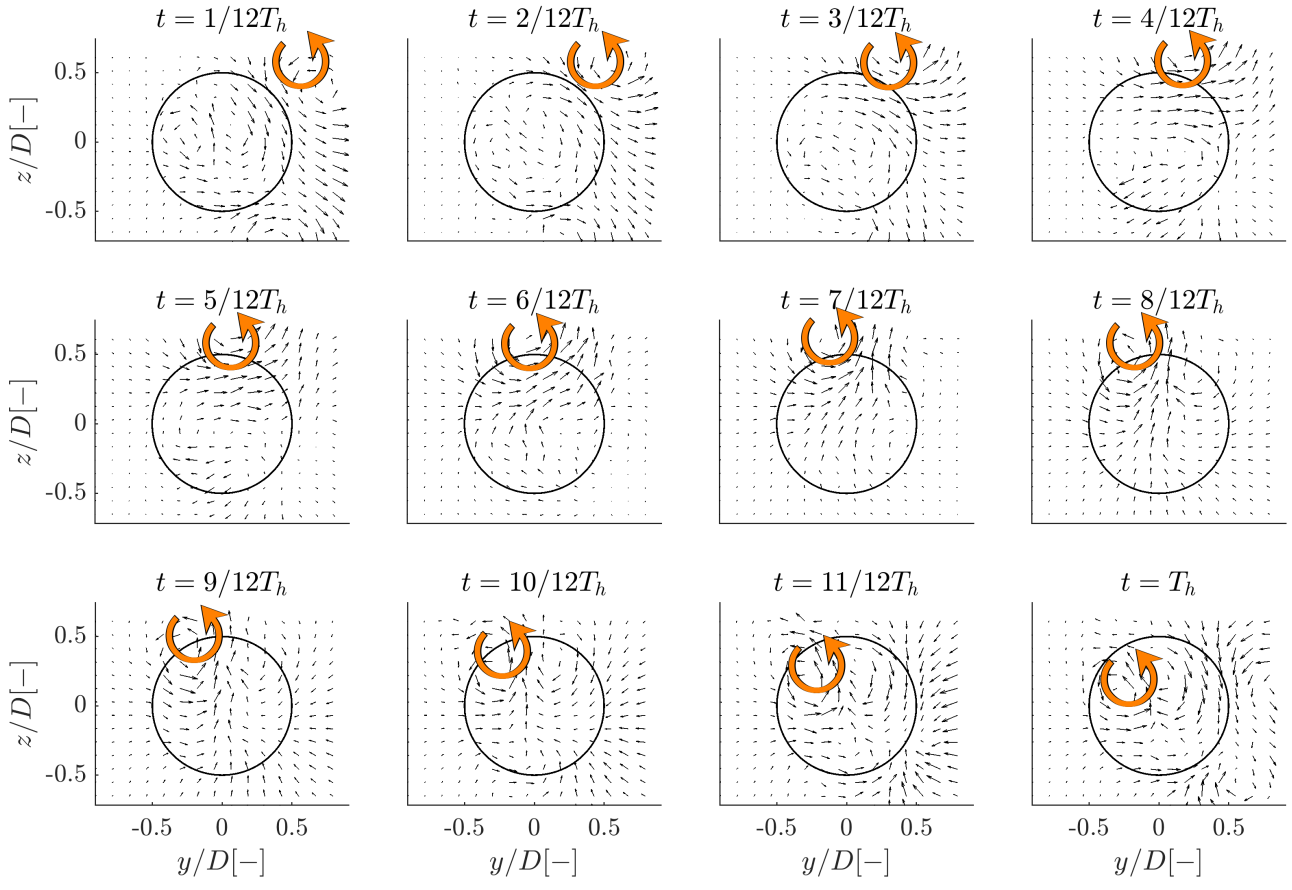


Figure 14. Binned planar velocity fields for the combination of helix and steering with negative yaw angle on a plane parallel to the rotor at $x/D = 3$ obtained with LES-ALM. View of an observer looking upstream. Different times t are reported as a fraction of the period of the helix, T_{helix}. Counterclockwise vortex centers are detected using the Γ_1 algorithm by Graftieaux et al. (2001) and shown with orange arrow markers. The perimeter of the rotor is shown with a black circle for reference.

https://doi.org/10.5194/wes-2026-214
Preprint. Discussion started: 19 November 2026
© Author(s) 2026. CC BY 4.0 License.

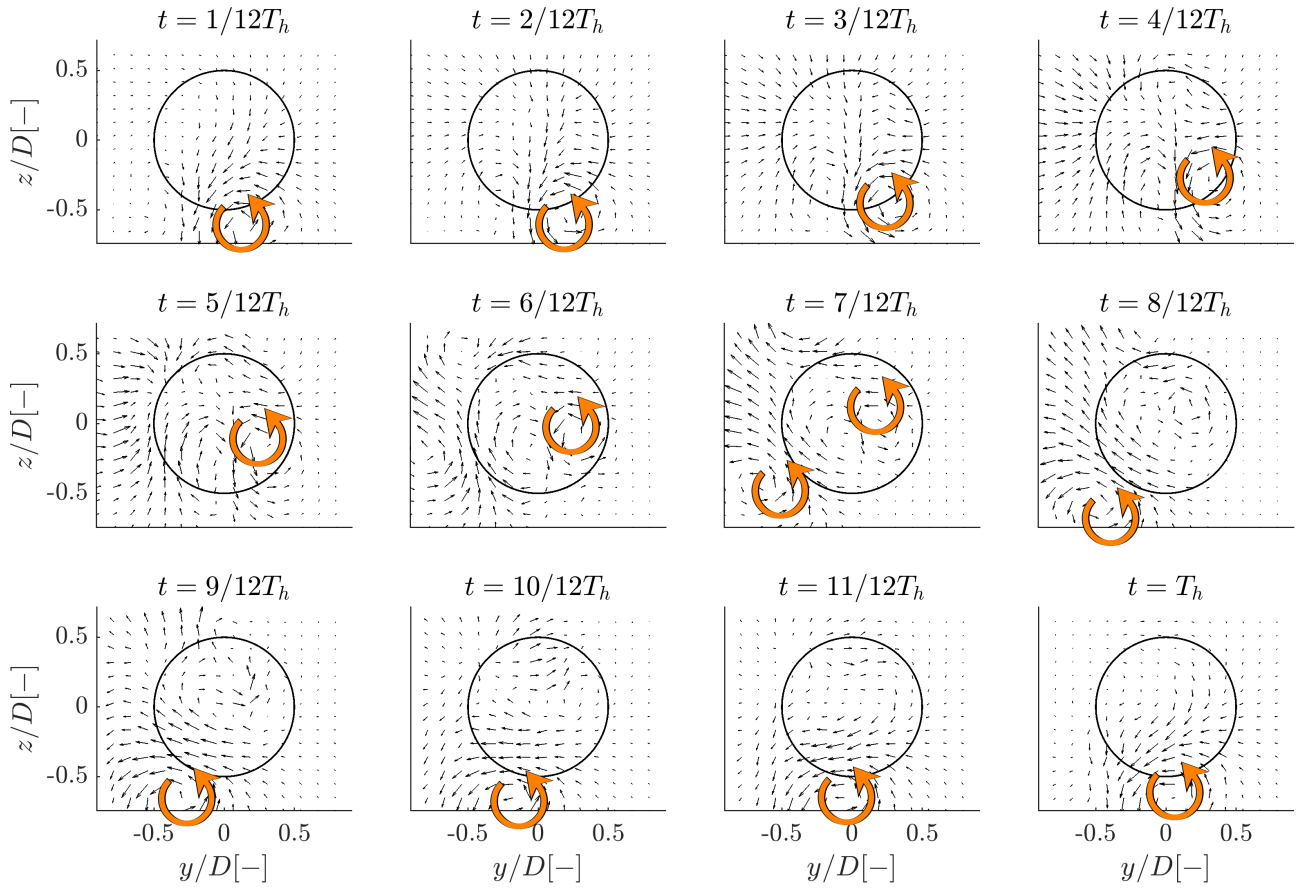


Figure 15. Binned planar velocity fields for the combination of helix and steering with positive yaw angle on a plane parallel to the rotor at $x/D = 3$ obtained with LES-ALM. View of an observer looking upstream. Different times t are reported as a fraction of the period of the helix, T_{helix}. Counterclockwise vortex centers are detected using the Γ_1 algorithm by Graftieaux et al. (2001) and shown with orange arrow markers. The perimeter of the rotor is shown with a black circle for reference.

https://doi.org/10.5194/wes-2026-214
Preprint. Discussion started: 19 November 2026
© Author(s) 2026. CC BY 4.0 License.



misalignment-induced vortices are always spinning in two opposite directions, there will always be this constructive-destructive interaction with the helix orbiting vortex, regardless of the direction of the helix and of the misalignment.

4 Conclusions

Wind tunnel experiments were conducted to investigate whether the power benefits of helix control and wake steering can be combined. The results show that, despite the apparent complementarity of the two strategies, their effects do not combine constructively: the simultaneous application of helix control and wake steering provides no additional wind-farm power benefit compared with the individual strategies.

The turbine power measurements show that the power losses of the upstream turbine due to blade pitch actuation and rotor misalignment combine approximately linearly, whereas the power gains of the downstream turbine obtained from the two strategies individually do not accumulate when they are applied simultaneously. Consequently, assuming that the effects of wake steering and wake mixing can be combined independently can lead to overly optimistic predictions of the achievable power gain.

The three-dimensional flow measurements reveal the physical mechanism underlying this behavior. Wake steering generates a pair of counter-rotating vortices, while helix control generates an outer vortex that orbits the wake. When the two strategies are combined, the orbiting helix vortex interacts with both steering vortices. This interaction produces a strong local amplification of circulation when vortices of the same sign approach one another, and a local reduction when their signs are opposite, substantially altering the trajectory and propagation of the helix vortex. Simultaneously, the interaction disrupts the balance of the steering vortex pair, weakening the lateral jet responsible for wake deflection. Thus, although the local constructive and destructive interactions occur during different portions of the helix cycle, their effects do not simply cancel over a complete cycle. Instead, the interaction fundamentally modifies the coherent vortical structures responsible for both wake mixing and wake steering. This provides a clear physical explanation for the reduced mixing and deflection observed when the two strategies are applied simultaneously.

These findings highlight that the apparently straightforward combination of wake steering and wake mixing in reality does involve non-trivial interactions between their underlying flow structures. The combined experimental and numerical results provide a physical basis for accounting for these interactions in the development and modeling of combined wake-control strategies.

https://doi.org/10.5194/wes-2026-214
Preprint. Discussion started: 19 November 2026
© Author(s) 2026. CC BY 4.0 License.



eawe european academy of wind energy
Open Access WIND ENERGY SCIENCE DISCUSSIONS

Appendix A: Wind tunnel campaign I: wind farm performance with variable rotational speed control on WT_1

Figure A1 shows the individual and combined power output of two aligned G1s and their combined power in the boundary-layer wind tunnel for the case of variable rotational speed operation of WT_1. The power values are presented for three control strategies and are normalized with respect to the baseline case, in which the upstream turbine operates at maximum efficiency. The expected power is indicated by a black dashed outline, and it is computed as mentioned in Sect. 3.1.

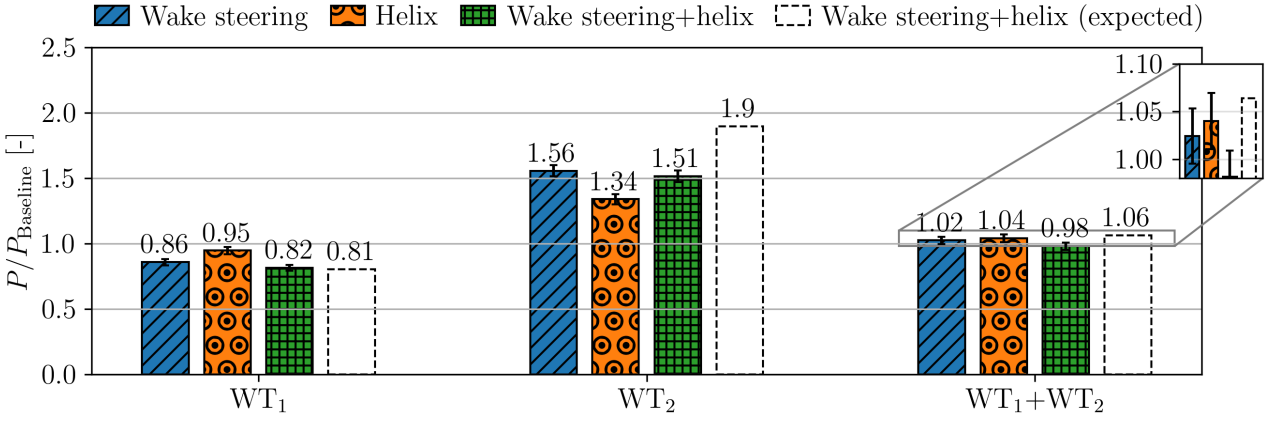


Figure A1. Local and collective power of two G1s in the boundary layer wind tunnel at Politecnico di Milano. The rotors are aligned at a distance of $5D$. Three control strategies are shown, and the data are normalized with the power measured with the baseline control method. WT_1 operates with variable RPM, following a $K\Omega^2$ approach for the generator torque, while WT_2 is controlled for maximum C_P. The expected performance of combined wake steering and helix, obtained by linearly summing the single techniques, is shown with a dashed black bar.

The performance of the controllers is similar to the case where WT_1 is operated at constant RPM (shown in Fig. 3): the combination of wake steering and helix performs below expectations. Power losses on WT_1 combine as expected, but once again, the power gains on WT_2 observed with helix and wake steering do not sum up.

Appendix B: Wake cross-section at $x/D = 3$ with LES-ALM for pure helix

Figure B1 presents the velocity field at a plane located at $x/D = 3$, alongside the position of the outer vortex, binned for different portions of the period of the helix. The figure shows a clear counterclockwise orbit of the outer vortex of the helix, occurring approximately along the perimeter of the rotor.

https://doi.org/10.5194/wes-2026-214
Preprint. Discussion started: 19 November 2026
© Author(s) 2026. CC BY 4.0 License.

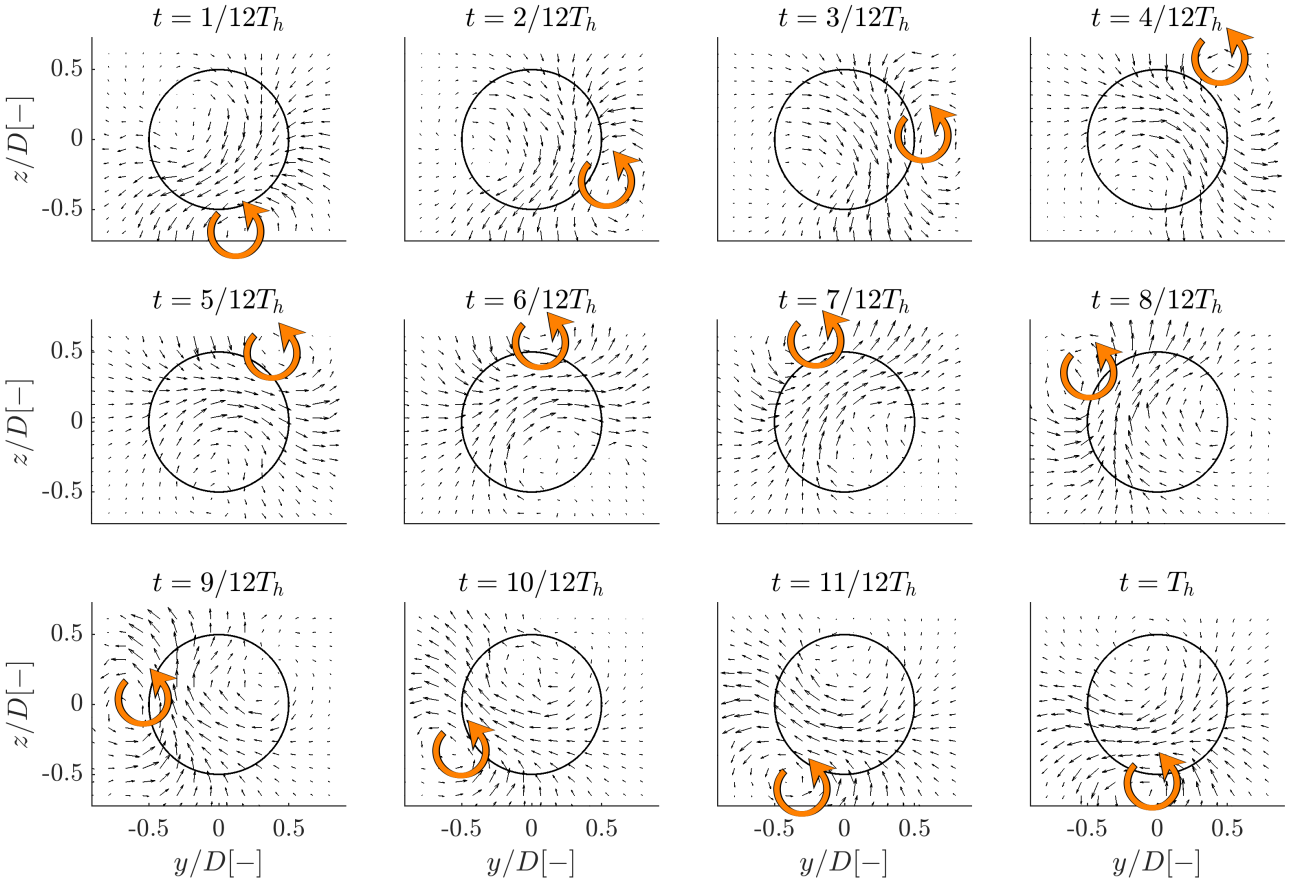


Figure B1. Binned planar velocity fields for the helix case on a plane parallel to the rotor at $x/D = 3$ obtained with LES-ALM. View of an observer looking upstream. Different times t are reported as a fraction of the period of the helix, T_{helix}. Counterclockwise vortex centers are detected using the Γ_1 algorithm by Graftieaux et al. (2001) and shown with orange arrow markers. The perimeter of the rotor is shown with a black circle for reference.

https://doi.org/10.5194/wes-2026-214
Preprint. Discussion started: 19 November 2026
© Author(s) 2026. CC BY 4.0 License.



eawe european academy of wind energy
Open Access WIND ENERGY SCIENCE DISCUSSIONS

Appendix C: Nomenclature

A	Amplitude of the pitch sinusoid of the helix
C_s	Smagorinsky subgrid scale model constant
D	Rotor diameter
K	Coefficient of the aerodynamic torque controller
k	Fraction of the rotational frequency used for the pitch sinusoid of the helix
P	Wind turbine power
P_R	Wind turbine rated power
R	Rotor radius
T_a	Acquisition time
T_h	Period of the helix
T_r	Period of the spinning rotor
t	Time
U_∞	Freestream wind speed
u	Streamwise velocity
v	Lateral velocity
w	Vertical velocity
x	Streamwise coordinate
y	Lateral coordinate
z	Vertical coordinate
$\boldsymbol{\beta}$	Blade pitch angle
β_OPT	Optimal blade pitch angle for maximum efficiency
Δx	LES-ALM mesh cell size at the rotor
ϵ	LES-ALM Gaussian projection radius
Γ	Circulation
γ	Yaw misalignment angle
λ	Tip speed ratio
ρ	Air density
ψ	Wind direction
Ω_R	Rated rotor angular speed
ω	Vorticity
FLORIS	FLOw Redirection and Induction in Steady State

https://doi.org/10.5194/wes-2026-214
Preprint. Discussion started: 19 November 2026
© Author(s) 2026. CC BY 4.0 License.

IPC	Individual pitch control
LES-ALM	Large eddy simulations with actuator line model
LPT	Lagrangian particle tracking velocimetry
RPM	Revolutions per minute
WT	Wind turbine

Code and data availability. The data needed to reproduce the figures is available on Zenodo at https://doi.org/10.5281/zenodo.23664327 (Tamaro et al., 2026). The full LPT dataset is available upon request.

Video supplement. A video of Figs. 4-7 is available at: https://youtu.be/j5RloNF93w8. The video for Figs. 10 and 11 can be accessed via the following link: https://youtu.be/BgF-UREulio.

Author contributions. CLB conceived the study and proposed the experimental campaigns. FVM, AS, and MM coordinated the experimental campaign. FC supported the development and implementation of the controllers. DB, ST, BD, İA, FVM performed the experiments. BD processed the LPT data. DB and ST processed the G1 signals. FVM, ST, and İA generated the figures. All authors contributed to the interpretation of the results. ST, FVM, and CLB wrote the paper. All authors provided important input to this research work through discussions and feedback, and improved the manuscript.

Competing interests. At least one of the (co-)authors is a member of the editorial board of *Wind Energy Science*.

Financial support. This work has been supported by the project "Twin Wind tunnels for Energy and the EnvironmenT - Innovations and Excellence" (TWEET-IE). TWEET-IE receives funding from the European Union's Horizon Europe Programme under grant agreement no. 101079125. The funding of the present investigations by the Deutsche Forschungsgemeinschaft (DFG, grant number BR 1511/20-1) under the "WakeAware" project (no. 531570398) is also gratefully acknowledged.

Acknowledgements. The authors express their gratitude to the Leibniz Supercomputing Centre (LRZ) for providing access and computing time on the SuperMUC Petascale System under Projekt-ID pn67qi "Large-eddy Simulation of wind farm Control beyond Power maximization" (LESCoP).

https://doi.org/10.5194/wes-2026-214
Preprint. Discussion started: 19 November 2026
© Author(s) 2026. CC BY 4.0 License.



eawe european academy of wind energy
Open Access WIND ENERGY SCIENCE DISCUSSIONS

References

Agüera, N., Cafiero, G., Astarita, T., and Discetti, S.: Ensemble 3D PTV for high resolution turbulent statistics, Measurement Science and Technology, 27, 124 011, 2016.

Bartl, J., Mühle, F., Schottler, J., Sætran, L., Peinke, J., Adaramola, M., and Hölling, M.: Wind tunnel experiments on wind turbine wakes in yaw: effects of inflow turbulence and shear, Wind Energy Science, 3, 329–343, https://doi.org/10.5194/wes-3-329-2018, 2018.

Bastankhah, M. and Porté-Agel, F.: Experimental and theoretical study of wind turbine wakes in yawed conditions, Journal of Fluid Mechanics, 806, 506–541, https://doi.org/10.1017/jfm.2016.595, 2016.

Bortolin, D., Tamaro, S., Campagnolo, F., Mühle, F. V., Manolesos, M., Croce, A., and Bottasso, C. L.: An experimental investigation on wake mixing and steering techniques, Journal of Physics: Conference Series, 3224, 032 050, https://doi.org/10.1088/1742-6596/3224/3/032050, 2026.

Bottasso, C. L. and Campagnolo, F.: Wind Tunnel Testing of Wind Turbines and Farms, in: Handbook of Wind Energy Aerodynamics, edited by Stoevesandt, B., Schepers, G., Fuglsang, P., and Sun, Y., pp. 1077–1126, Springer International Publishing, Cham, ISBN 978-3-030-31307-4, https://doi.org/10.1007/978-3-030-31307-4_54, 2022.

Branlard, E. and Gaunaa, M.: Cylindrical vortex wake model: skewed cylinder, application to yawed or tilted rotors, Wind Energy, 19, 345–358, https://doi.org/10.1002/we.1838, 2016.

Cal, R. B., Lebrón, J., Castillo, L., Kang, H. S., and Meneveau, C.: Experimental study of the horizontally averaged flow structure in a model wind-turbine array boundary layer, Journal of Renewable and Sustainable Energy, 2, 013 106, https://doi.org/10.1063/1.3289735, 2010.

Campagnolo, F., Aktan, H. D., Bortolin, D., Tamaro, S., Mühle, F. V., and Bottasso, C. L.: Experimental wind tunnel dataset of wake and turbine measurements for wind farm control, Wind Energy Science, 11, 4005–4040, https://doi.org/10.5194/wes-11-4005-2026, 2026.

Canet, H., Bortolotti, P., and Bottasso, C. L.: On the scaling of wind turbine rotors, Wind Energy Science, 6, 601–626, https://doi.org/10.5194/wes-6-601-2021, 2021.

Coquelet, M., Gutknecht, J., van Wingerden, J.-W., Duponcheel, M., and Chatelain, P.: Dynamic individual pitch control for wake mitigation: Why does the helix handedness in the wake matter?, Journal of Physics: Conference Series, 2767, 092 084, https://doi.org/10.1088/1742-6596/2767/9/092084, 2024.

Doekemeijer, B. M., Kern, S., Maturu, S., Kanev, S., Salbert, B., Schreiber, J., Campagnolo, F., Bottasso, C. L., Schuler, S., Wilts, F., Neumann, T., Potenza, G., Calabretta, F., Fioretti, F., and van Wingerden, J.-W.: Field experiment for open-loop yaw-based wake steering at a commercial onshore wind farm in Italy, Wind Energy Science, 6, 159–176, https://doi.org/10.5194/wes-6-159-2021, 2021.

Faleiros, D., Tuinstra, M., Sciacchitano, A., and Scarano, F.: Generation and control of helium-filled soap bubbles for PIV, Experiments in Fluids, 60, https://doi.org/10.1007/s00348-019-2687-4, 2019.

Fleming, P. A., Gebraad, P. M., Lee, S., van Wingerden, J.-W., Johnson, K., Churchfield, M., Michalakes, J., Spalart, P., and Moriarty, P.: Evaluating techniques for redirecting turbine wakes using SOWFA, Renewable Energy, 70, 211–218, https://doi.org/https://doi.org/10.1016/j.renene.2014.02.015, special issue on aerodynamics of offshore wind energy systems and wakes, 2014.

Frederik, J. A., Doekemeijer, B. M., Mulders, S. P., and van Wingerden, J.-W.: The helix approach: Using dynamic individual pitch control to enhance wake mixing in wind farms, Wind Energy, 23, 1739–1751, https://doi.org/https://doi.org/10.1002/we.2513, 2020.

https://doi.org/10.5194/wes-2026-214
Preprint. Discussion started: 19 November 2026
© Author(s) 2026. CC BY 4.0 License.



Frederik, J. A. A.: Pitch control for wind turbine load mitigation and enhanced wake mixing: A simulation and experimental validation study, Ph.D. thesis, Delft University of Technology, Delft, The Netherlands, ISBN 9789463663731, https://doi.org/10.4233/uuid:09e98a0c-65f8-46d3-b356-459987c0228a, doctoral dissertation, Team Jan-Willem van Wingerden, 2021.

Gebraad, P. M. O., Teeuwisse, F. W., van Wingerden, J. W., Fleming, P. A., Ruben, S. D., Marden, J. R., and Pao, L. Y.: Wind plant power optimization through yaw control using a parametric model for wake effects—a CFD simulation study, Wind Energy, 19, 95–114, https://doi.org/https://doi.org/10.1002/we.1822, 2016.

Graftieaux, L., Michard, M., and Grosjean, N.: Combining PIV, POD and vortex identification algorithms for the study of unsteady turbulent swirling flows, Measurement Science and Technology, 12, 1422, https://doi.org/10.1088/0957-0233/12/9/307, 2001.

Gutknecht, J., Taschner, E., Coquelet, M., Viré, A., and van Wingerden, J.-W.: The impact of coherent large-scale vortices generated by helix active wake control on the recovery process of wind turbine wakes, Physics of Fluids, 37, https://doi.org/10.1063/5.0278687, 2025a.

Gutknecht, J., van den Berg, D., van der Hoek, D., De Vos, B., Harder, B., Viré, A., and van Wingerden, J.-W.: Wake Recovery Enhancement with Helix Active Wake Control: Vortex Structures in a Porous Disk Wake Observed in PIV Experiments, Journal of Physics: Conference Series, 3016, 012 030, https://doi.org/10.1088/1742-6596/3016/1/012030, 2025b.

Hansen, M.: Aerodynamics of wind turbines: Third edition, Routledge, ISBN 9781315769981, https://doi.org/10.4324/9781315769981, 2015.

Howland, M. F., Bossuyt, J., Martínez-Tossas, L. A., Meyers, J., and Meneveau, C.: Wake structure in actuator disk models of wind turbines in yaw under uniform inflow conditions, Journal of Renewable and Sustainable Energy, 8, 043 301, https://doi.org/10.1063/1.4955091, 2016.

Jiménez, A., Crespo, A., and Migoya, E.: Application of a LES technique to characterize the wake deflection of a wind turbine in yaw, Wind Energy, 13, 559–572, https://doi.org/https://doi.org/10.1002/we.380, 2010.

Jonkman, B. J.: TurbSim User's Guide, Version 2.00.00, Tech. rep., National Renewable Energy Laboratory (NREL), Golden, CO, 2016.

Kuhn, M. B., Henry de Frahan, M. T., Mohan, P., Deskos, G., Churchfield, M., Cheung, L., Sharma, A., Almgren, A., Ananthan, S., Brazell, M. J., Martínez-Tossas, L. A., Thedin, R., Rood, J., Sakievich, P., Vijayakumar, G., Zhang, W., and Sprague, M.: AMR-Wind: A Performance-Portable, High-Fidelity Flow Solver for Wind Farm Simulations, Wind Energy, 28, e70 010, https://doi.org/https://doi.org/10.1002/we.70010, 2025.

Lignarolo, L., Ragni, D., Krishnaswami, C., Chen, Q., Simão Ferreira, C., and van Bussel, G.: Experimental analysis of the wake of a horizontal-axis wind-turbine model, Renewable Energy, 70, 31–46, https://doi.org/https://doi.org/10.1016/j.renene.2014.01.020, special issue on aerodynamics of offshore wind energy systems and wakes, 2014.

Medici, D. and Alfredsson, P. H.: Measurements on a wind turbine wake: 3D effects and bluff body vortex shedding, Wind Energy, 9, 219–236, https://doi.org/https://doi.org/10.1002/we.156, 2006.

Mühle, F. V., Heckmeier, F. M., Campagnolo, F., and Breitsamter, C.: Wind tunnel investigations of an individual pitch control strategy for wind farm power optimization, Wind Energy Science, 9, 1251–1271, https://doi.org/10.5194/wes-9-1251-2024, 2024.

NREL: OpenFAST, https://github.com/openfast, accessed 19 March 2023, 2023.

Sagaut, P.: Large Eddy Simulation for Incompressible Flows: An Introduction, Scientific Computation, Springer, Berlin, https://doi.org/10.1007/b137536, 2006.

Scarano, F., Ghaemi, S., Caridi, G., Bosbach, J., Dierksheide, U., and Sciacchitano, A.: On the use of helium-filled soap bubbles for large-scale tomographic PIV in wind tunnel experiments, Experiments in Fluids, 56, 42, https://doi.org/10.1007/s00348-015-1909-7, 2015.

https://doi.org/10.5194/wes-2026-214
Preprint. Discussion started: 19 November 2026
© Author(s) 2026. CC BY 4.0 License.



Schanz, D., Gesemann, S., and Schröder, A.: Shake-The-Box: Lagrangian particle tracking at high particle image densities, Experiments in fluids, 57, 70, 2016.

Shapiro, C. R., Gayme, D. F., and Meneveau, C.: Generation and decay of counter-rotating vortices downstream of yawed wind turbines in the atmospheric boundary layer, Journal of Fluid Mechanics, 903, R2, https://doi.org/10.1017/jfm.2020.717, 2020.

Tamaro, S., Mühle, F. V., Dsouza, B., Bortolin, D., Alagöz, I., Campagnolo, F., Manolesos, M., Sciacchitano, A., and Bottasso, C. L.: Combined wake steering and helix control: why power gains are not additive, https://doi.org/10.5281/zenodo.23664328, 2026.

Taschner, E., Becker, M., Verzijlbergh, R., and van Wingerden, J.-W.: Comparison of helix and wake steering control for varying turbine spacing and wind direction, Journal of Physics: Conference Series, 2767, 032 023, https://doi.org/10.1088/1742-6596/2767/3/032023, 2024.

Troldborg, N., Sørensen, J. N., Mikkelsen, R., and Sørensen, N. N.: A simple atmospheric boundary layer model applied to large eddy simulations of wind turbine wakes, Wind Energy, 17, 657–669, https://doi.org/https://doi.org/10.1002/we.1608, 2014.

van den Berg, D., de Tavernier, D., and van Wingerden, J.-W.: Using the Helix Mixing Approach on Floating Offshore Wind Turbines, Journal of Physics: Conference Series, 2265, 042 011, https://doi.org/10.1088/1742-6596/2265/4/042011, 2022.

van der Hoek, D., van den Abbeele, B., Simao Ferreira, C., and van Wingerden, J.-W.: Maximizing wind farm power output with the helix approach: Experimental validation and wake analysis using tomographic particle image velocimetry, Wind Energy, 27, 463–482, https://doi.org/https://doi.org/10.1002/we.2896, 2024.

van Vondelen, A. A. W., Coquelet, M., Navalkar, S. T., and van Wingerden, J.-W.: Synchronized Helix wake mixing control, Wind Energy Science, 10, 2411–2433, https://doi.org/10.5194/wes-10-2411-2025, 2025.

Wang, C., Campagnolo, F., and Bottasso, C. L.: Identification of airfoil polars from uncertain experimental measurements, Wind Energy Science, 5, 1537–1550, https://doi.org/10.5194/wes-5-1537-2020, 2020.

Wang, C., Campagnolo, F., Canet, H., Barreiro, D. J., and Bottasso, C. L.: How realistic are the wakes of scaled wind turbine models?, Wind Energy Science, 6, 961–981, https://doi.org/10.5194/wes-6-961-2021, 2021.